HEAVY QUARK PRODUCTION IN HEAVY-ION COLLISIONS

by

Peter Michael Valerio, Jr.

A Dissertation Submitted to the Faculty of the

DEPARTMENT OF PHYSICS

In Partial Fulfillment of the Requirements
For the Degree of

DOCTOR OF PHILOSOPHY

In the Graduate College

THE UNIVERSITY OF ARIZONA

1 9 9 6

INFORMATION TO USERS

This manuscript has been reproduced from the microfilm master. UMI films the text directly from the original or copy submitted. Thus, some thesis and dissertation copies are in typewriter face, while others may be from any type of computer printer.

The quality of this reproduction is dependent upon the quality of the copy submitted. Broken or indistinct print, colored or poor quality illustrations and photographs, print bleedthrough, substandard margins, and improper alignment can adversely affect reproduction.

In the unlikely event that the author did not send UMI a complete manuscript and there are missing pages, these will be noted. Also, if unauthorized copyright material had to be removed, a note will indicate the deletion.

Oversize materials (e.g., maps, drawings, charts) are reproduced by sectioning the original, beginning at the upper left-hand corner and continuing from left to right in equal sections with small overlaps. Each original is also photographed in one exposure and is included in reduced form at the back of the book.

Photographs included in the original manuscript have been reproduced xerographically in this copy. Higher quality 6" x 9" black and white photographic prints are available for any photographs or illustrations appearing in this copy for an additional charge. Contact UMI directly to order.

UMI

A Bell & Howell Information Company
300 North Zeeb Road, Ann Arbor MI 48106-1346 USA
313/761-4700 800/521-0600

HEAVY QUARK PRODUCTION IN HEAVY-ION COLLISIONS

by

Peter Michael Valerio, Jr.

A Dissertation Submitted to the Faculty of the

DEPARTMENT OF PHYSICS

In Partial Fulfillment of the Requirements
For the Degree of

DOCTOR OF PHILOSOPHY

In the Graduate College

THE UNIVERSITY OF ARIZONA

1 9 9 6

THE UNIVERSITY OF ARIZONA ®
GRADUATE COLLEGE

As members of the Final Examination Committee, we certify that we have read the dissertation prepared by Peter Michael Valerio, Jr.

entitled Heavy Quark Production in Heavy-Ion Collisions

and recommend that it be accepted as fulfilling the dissertation requirement for the Degree of Doctor of Philosophy

I. Sarcevic	11/19/1996 Date
D. Toussaint	11/19/96 Date
B.R. Barrett	11/19/96 Date
T. Bowen	11/19/96 Date
M.A. Shupe	11/19/96 Date

Final approval and acceptance of this dissertation is contingent upon the candidate's submission of the final copy of the dissertation to the Graduate College.

I hereby certify that I have read this dissertation prepared under my direction and recommend that it be accepted as fulfilling the dissertation requirement.

Dissertation Director I. Sarcevic	11/19/1996 Date

STATEMENT BY AUTHOR

This dissertation has been submitted in partial fulfillment of requirements for an advanced degree at The University of Arizona and is deposited in the University Library to be made available to borrowers under rules of the library.

Brief quotations from this dissertation are allowable without special permission, provided that accurate acknowledgment of source is made. Requests for permission for extended quotation from or reproduction of this manuscript in whole or in part may be granted by the head of the major department or the Dean of the Graduate College when in his or her judgment the proposed use of the material is in the interests of scholarship. In all other instances, however, permission must be obtained from the author.

SIGNED: 

Acknowledgments

For, the last several years, I was lucky enough to have worked with someone who taught me a great deal, both professionally and personally. In my tenure as her student, Dr. Ina Sarcevic tried to keep me focused on problems that would be interesting to people other than me. To say that I wouldn't have been able to get through this experience without her guidance would be an understatement.

In the past year, I had the good fortune to meet Dr. Zheng Huang. I learned more physics from him than he suspects, I suspect. He is a brilliant young physicist who seems to be a jack of all trades. I am deeply indebted to him, and I will remember him as my dearest collaborators.

I thank my lucky stars that I was a friend of Dr. David 'Larry' Fein before I worked with him. In the last 6-9 months, I made him waste more CPU time than any reasonable person would ever use. Without him the dimuon spectra would never have been calculated. He is truly a *mensch.*

I also need to thank someone who could best be described as my longterm male companion, that is, if that phrase wasn't a euphemism for something else. Dr. Michael Chandross helped me to deal with the monotony. He helped me to take the edge off. He's the only human that even challenges me at backgammon. I let him win a few, so he'll keep playing.

Many people in this department don't realize that if you want your time here to go smoothly, you have to be on Iris Wright's good side. I would never have been able to defend without Iris. She is the heart of this department. I am also indebted to Donna Kent. She helped me proofread the document you hold in front of you. She is a dear friend.

For emotional support, no one has helped me more than my wife, Amy. She put up with my shenanigans for longer than I can remember. She helped my through my doubts, my insecurities, and my despair. I could never have finished this if it weren't for her.

Finally, I want to thank my parents for allowing me to pursue my interest, and not making me become an accountant.

Dedication

I want to dedicate this dissertation to two men who meant a lot to me: Peter Arthur Valerio and Joseph Francis Pozniak. Unfortunately, you both passed on before I finished. You are both in my heart always.

"The schools of Hillel and Shammai disputed two and a half years whether it would have been better if man had or had not been created. Finally they agreed it would have been better had he not been created, but since he has been created, let him investigate his past doings and let him examine what he is about to do."

Babylonian Talmud/Erubim

TABLE OF CONTENTS

LIST OF FIGURES

LIST OF TABLES

ABSTRACT

The results of the full next to leading order calculation of open charm production cross section, via hard parton scattering, for both hadronic and heavy-ion collisions at RHIC and LHC energies are presented. In addition to the total cross section, the transverse momentum and rapidity distributions are included. An effective K-factor which encapsulates the next to leading order corrections and the nuclear effects is presented.

The open charm yield will be measured through the correlated dileptons produced when the charm decays. An important background comes from the decay of bottom quarks. Therefore, the open bottom yield from hard parton scatterings is presented.

The first next to leading order calculation of the thermal heavy quark production is presented, as well as the dimuon spectrum from both the thermal and the initial fusion charm and bottom production at RHIC energies.

CHAPTER 1

Introduction

1.1 Heavy-Ion Physics

The field of heavy-ion physics is centered on the study of high-energy nucleus-nucleus collisions. The large amounts of energy, deposited in small regions of phase space in these collisions, present researchers with an opportunity to observe signatures of new physics. It has been speculated that the high energy densities achieved at the extreme conditions present during a nucleus-nucleus collision [1] will be sufficient to allow a phase transition from normal hadronic matter to a thermal system of deconfined quarks and gluons, the so-called quark gluon plasma.

An estimate of the energy density achievable in nuclear collisions was made by Bjorken, who reconstructed the initial distribution of energy density by examining the energy and number of produced hadrons. These calculations began with the head-on collision of two like nuclei, moving near the speed of light, one from $z = -\infty$ and the other from $z = \infty$, in the center-of-mass frame. The collision takes place at time $t = 0$ and longitudinal position $z = 0$. If the center-of-mass energy for the collision is sufficiently high, there will be considerable Lorentz contraction in the longitudinal direction. At high energy, a nucleus-nucleus collision is effectively the collision of two thin discs. Thus, the longitudinal component for each nucleon in a nucleus is the same. The energy lost by the incident nuclei in this collision will be deposited in a volume, $\aleph\Delta z$, where $\aleph$ is the transverse area of the nuclear disc and Δz is a length that typifies the longitudinal size of the interaction

region. The energy deposited will be carried by quarks, gluons, or hadrons. Regardless of the quanta that carry the energy in the interaction region, the particles that are detected are mainly charged pions with transverse momentum of about 350 MeV.

Consider the following kinematic variables. In a collider experiment, there is usually azimuthal symmetry, so it is natural to separate the longitudinal component of the momentum, p_z, from the transverse components of the momentum, $\mathbf{p}_\perp$. The mass shell condition constrains the energy of the particle, so that the four-momentum is fully defined by just three independent variables. It is convenient to use as the independent variables the particle rapidity, y, transverse momentum, $p_\perp$, and azimuthal angle, ϕ. The rapidity variable is defined as

$$y \equiv \frac{1}{2}\ln(\frac{p_0 + p_z}{p_0 - p_z}), \tag{1.1}$$

where p_0 is the particle energy. Using these variables, the four momentum can be written

$$p^\mu = (m_T \cosh y, p_\perp \cos\phi, p_\perp \sin\phi, m_T \sinh y), \tag{1.2}$$

where m_T is the transverse mass, given by

$$m_T^2 = m^2 + p_\perp^2, \tag{1.3}$$

where m is the mass of the particle. The rapidity variable is especially useful in that boosts in the longitudinal direction amount to additive factors to the rapidity.

An estimate of the energy density, ϵ_0, in the space-time region where the collision occurs, can be made by determining the energy of all of the particles that are produced in that volume. Assuming that all of the energy is carried out by the pions produced, and each pion has the same energy, the energy density can be estimated as:

$$\epsilon_0 = p^0 \frac{\Delta N}{\aleph \Delta z} = m_T \cosh y \frac{\Delta N}{\aleph \Delta z}, \tag{1.4}$$

where $\frac{\Delta N}{\aleph \Delta z}$ is the number of pions produced in the collision volume. A relationship between space-time variables and momentum variables must be found. The ratio

$$\frac{p_z}{p^0} = \frac{\gamma \beta_z m}{\gamma m} = \beta_z, \tag{1.5}$$

where β_z is the longitudinal speed of the particle. Also,

$$\frac{p_z}{p^0} = \tanh y, \tag{1.6}$$

so

$$\beta_z = \frac{z}{t} = \tanh y. \tag{1.7}$$

Thus, these space-time co-ordinates can be written in terms of the rapidity variable:

$$z = \tau \sinh y, \tag{1.8}$$

and

$$t = \tau \cosh y, \tag{1.9}$$

where $\tau = \sqrt{t^2 - z^2}$ is the proper time. For a finite τ, z near 0 corresponds to y near 0, the so-called central rapidity region. Therefore, the important pions will have rapidity nearly 0.

The number of pions produced in the collision volume can be written in terms of the pion rapidity distribution, dN/dy

$$\frac{\Delta N}{\aleph \Delta z} = \frac{1}{\aleph} \frac{dN}{dy} \frac{dy}{dz} \tag{1.10}$$

$$= \frac{1}{\aleph} \frac{dN}{dy} \frac{1}{\tau \cosh y} \tag{1.11}$$

at $y = 0$. So, the energy density attainable in a central nucleus-nucleus collision is

$$\epsilon_0 = \frac{m_T}{\tau \aleph} \frac{dN}{dy}|_{y=0}. \tag{1.12}$$

To get a numerical estimate, the average transverse mass of the produced pions is 380 MeV, and the transverse area $\aleph = \pi(1.2)^2 A^{2/3}$ fm^2 for atomic number A. From fixed target experiments [2], of 200 GeV per nucleon ^{32}S on a number of different target nuclei, the pion rapidity distributions were found to be on the order of 150 pions per unit of rapidity. The energy density is estimated to be a few GeV/fm^3, which may be sufficient to create a quark-gluon plasma.

1.2 The Quark-Gluon Plasma (QGP)

It is generally accepted that QCD describes the dynamics governing the binding of quarks into hadrons. Since the length scale is on the order of the size of a hadron rather than the size of a parton, the physics is non-perturbative. A phenomonological model for these bound states, the MIT bag model [3], leads to some interesting results. This model, in essence, assumes that quarks are massless particles confined to a region of physical space the size of a hadron. It further assumes that there is an inward pressure, the bag pressure, B, that keeps these partons confined to the hadron.

By solving the Dirac equation for massless free fermions in a spherical cavity, an estimate of the bag energy can be made. With the boundary condition that the quark density is equal to zero outside of the bag, the energy can be expressed in terms of the bag pressure and the size of the bag. The bag pressure can be estimated to be

$$B^{1/4} = 206\text{MeV}. \tag{1.13}$$

If the pressure of the system of quarks and gluons in the bag becomes greater than the bag pressure, these partons will no longer be confined to the bag. The system will experience a phase transition to a deconfined phase, the so-called quark-gluon plasma (QGP). This large pressure can be brought about by an increase in temperature or an increase in baryon number density. Based on the estimate of the bag pressure, the energy density for a QGP phase transition is on the order of a few GeV/fm^3. It is conceivable, therefore, that a high-energy heavy-ion collision will create this deconfined state.

Assume that an ideal system of quarks and gluons exists in thermal equilibrium at some temperature, T, in some volume, V. The pressure of this system can be determined from a simple statistical mechanics calculation. If the number of quarks is equal to the number of anti-quarks, the chemical potential of the quark

and the chemical potential of the anti-quark, μ_q and $\mu_{\bar{q}}$ respectively, can be taken to be zero. In this system, the net baryon number in the plasma is also zero.

The number of massless quarks with momentum between p and $p + dp$ is given by a Fermi-Dirac distribution,

$$dN_q = \frac{g_q V 4\pi p^2 dp}{(2\pi)^3}[\frac{1}{1+e^{p/T}}], \tag{1.14}$$

where g_q is the quark degeneracy factor determined by

$$g_q = N_c N_s N_f \tag{1.15}$$

where N_c is the number of colors, N_s is the number of spins, and N_f is the number of flavors. For 2 light flavors, the degeneracy factor, $g_q = 12$. The total energy of the massless quark gas is given by

$$\begin{aligned}
E_q &= \int p_0 dN_q && (1.16)\\
&= \frac{g_q V}{2\pi^2}\int_0^\infty \frac{p^3 dp}{1+e^{p/T}} && (1.17)\\
&= \frac{g_q V}{2\pi^2}T^4\int_0^\infty \frac{x^3 dx}{1+e^x} && (1.18)\\
&= \frac{g_q V}{2\pi^2}T^4\sum_{n=0}^\infty\int_0^\infty x^3 dx(-1)^n e^{-x}e^{-nx} && (1.19)\\
&= \frac{g_q V}{2\pi^2}T^4\sum_{n=0}^\infty\int_0^\infty x^3 dx(-1)^n e^{-(n+1)x} && (1.20)\\
&= \frac{g_q V}{2\pi^2}T^4\int_0^\infty z^3 dz e^{-z}\sum_{n=0}^\infty(-1)^n\frac{1}{(n+1)^4} && (1.21)\\
&= \frac{g_q V}{2\pi^2}T^4\Gamma(4)\sum_{n=0}^\infty(-1)^n\frac{1}{(n+1)^4}, && (1.22)
\end{aligned}$$

where Γ is the gamma function. The sum can be evaluated

$$\begin{aligned}
\sum_{n=0}^\infty(-1)^n\frac{1}{(n+1)^4} &= \sum_{m=1,3,5\ldots}\frac{1}{m^4} - \sum_{m=2,4,6\ldots}\frac{1}{m^4} && (1.23)\\
&= \sum_{m=1,2,3\ldots}\frac{1}{m^4} - 2\sum_{m=2,4,6\ldots}\frac{1}{m^4} && (1.24)
\end{aligned}$$

$$= \sum_{m=1,2,3...} \frac{1}{m^4} - 2 \sum_{m=1,2,3...} \frac{1}{(2m)^4} \tag{1.25}$$

$$= (1 - 2^{-3})\zeta(4) \tag{1.26}$$

$$= \frac{7}{8}\zeta(4), \tag{1.27}$$

where ζ is the Riemann zeta function. This zeta function has the value $\zeta(4) = \pi^4/90$, and the gamma function has the value $\Gamma(4) = 3! = 6$. The total energy of the quark gas is

$$E_q = \frac{7}{8} g_q V \frac{\pi^2}{30} T^4. \tag{1.28}$$

From a similar calculation, the total energy of the ideal anti-quark gas is found to be the same as 1.28, so the total energy in the quark sector is

$$E_{q\bar{q}} = \frac{7}{4} g_q V \frac{\pi^2}{30} T^4. \tag{1.29}$$

For massless non-interacting particles, the pressure is related to the energy by

$$P = \frac{1}{3}\frac{E}{V}. \tag{1.30}$$

Therefore, the pressure of the quark gas is

$$P_{q\bar{q}} = 21 \frac{\pi^2}{90} T^4. \tag{1.31}$$

To estimate the pressure of the plasma, the pressure due to the gluons must also be calculated. There are only two differences between this calculation and the calculation of the pressure from the quark gas. Gluons are bosons, so they obey Bose-Einstein statistics. Also, the degeneracy factor, g_g, is given by

$$g_g = N_c N_s, \tag{1.32}$$

where, for gluons, the number of color degrees of freedom is 8 and the number of spin polarizations is 2, yielding a degeneracy factor $g_g = 16$. The energy of the gluon gas is given by

$$E_g = \frac{g_g V}{2\pi^2} \int_0^\infty \frac{p^3 dp}{e^{p/T} - 1}. \tag{1.33}$$

Performing the integral yields

$$E_g = \frac{g_g V}{2\pi^2} T^4 \Gamma(4)\zeta(4) \tag{1.34}$$

$$= g_g V \frac{\pi^2}{30} T^4. \tag{1.35}$$

Thus, the pressure of the gluon gas, P_g is given

$$P_g = 16\frac{\pi^2}{90} T^4. \tag{1.36}$$

The total pressure of the system of noninteracting, massless quarks and gluons is the sum of the two pressures

$$P = P_{q\bar{q}} + P_g = 37\frac{\pi^2}{90} T^4. \tag{1.37}$$

If the temperature becomes so high that the pressure exceeds the bag pressure, B, the partons would no longer be confined to the hadron. Thus, the critical temperature for a deconfinement phase temperature can be estimated to be

$$T_c = (\frac{90}{37\pi^2})^{1/4} B^{1/4} \tag{1.38}$$

which is about $T_c \approx 144$ MeV. This corresponds to a critical energy density of about .7 GeV/fm^3, slightly lower than the energy densities expected at RHIC. This estimate suggests a strong likelihood that collisions at RHIC will produce the thermalized system.

1.3 Signals for a QGP

Once the possibility of producing the thermalized system has been established, the problem of finding a clean detectable signal must be resolved. Numerous signals have been proposed, from J/ψ suppression to strangeness enhancement, but the following discussion will be limited to dilepton production and open charm production, which have been the foci of our work.

1.3.1 Dilepton Production

The plasma will be made up of hot matter which interacts primarily via the strong interaction. Any proposed signal that carries color charge is very likely to be rescattered, and the signal will be lost before it reaches the detectors. In a plasma, a quark and an anti-quark can annihilate to form a virtual photon. This virtual photon can decay into a lepton anti-lepton pair, or dilepton. Leptons carry no color charge, so any produced leptons will interact with the QGP only through the electromagnetic interaction. The cross section for lepton-quark scattering is of the order $(\alpha/\sqrt{s})^2$, where $\alpha = 1/137$. It is unlikely that the produced leptons will interact with the plasma. However, the production rate and momentum distribution of the produced leptons depend on the momentum distribution of the quarks in the plasma, which in turn depends on the thermodynamics of the plasma.

The dilepton is characterized by the invariant mass, $M^2 = (p_l + p_{\bar{l}})^2$. It was previously believed that dileptons from the QGP will only be detected above the backgrounds for invariant masses 1-2 GeV. Below 1 GeV the hadronic backgrounds are expected to dominate [4], and above 2 GeV Drell-Yan pairs from the initial collision begin to dominate. The rapidity distributions of thermal dileptons at RHIC and LHC energies have been calculated [5]. The dileptons from charm decays are believed to provide a substantial contribution to the total dilepton spectrum, and thus provide an important background to the thermal dilepton signal. It was shown that the thermal charm yield would become significant if the initial plasma temperature was moderately high, $T_0 > 400$ MeV [6], and the dileptons from the thermal charm decays become significant at $T_0 \approx 500$ MeV [7].

1.3.2 Open Charm Production in a QGP

Because of the charm quark's mass, a charm pair can only be produced in a plasma at early times. As the plasma evolves in space-time, it expands and cools. Charm

quarks are more likely to be produced when the partons in the plasma are more energetic. Also, the charm density in the plasma will be quite low, so the chance of annihilation is very slight. Since the charm quark mass is so great, the cross section for charm interaction with light quarks is smaller than the light quark-light quark cross section. Open charm, charmed quarks that are not in a $c\bar{c}$ bound state, will very likely escape the plasma unscattered. Since the momentum distributions of the charm will depend on the thermodynamics of the plasma, specifically the initial temperature, open charm provides an attractive signal.

Open charm enhancement was first suggested as a plasma signature almost twenty years ago [8]. This enhancement was a direct consequence of Shuryak's hot glue scenario [9], outlined below. The parton level gluon-gluon to gluon-gluon cross section is large relative to the other subprocesses. The leading order, $O(\alpha_s^2)$, matrix elements can be calculated in perturbative QCD and found to be [10]:

$$M^2_{gg\to gg} = \frac{9}{2}(3 - \frac{ut}{s^2} - \frac{us}{t^2} - \frac{st}{u^2}), \tag{1.39}$$

$$M^2_{gg\to q\bar{q}} = \frac{1}{6}\frac{u^2+t^2}{ut} - \frac{3}{8}\frac{u^2+t^2}{s^2}, \tag{1.40}$$

$$M^2_{qg\to qg} = -\frac{4}{9}\frac{u^2+s^2}{us} + \frac{u^2+s^2}{t^2}, \tag{1.41}$$

$$M^2_{q_1q_2\to q_1q_2} = \frac{4}{9}\frac{s^2+u^2}{t^2}, \tag{1.42}$$

where s, t, and u are the usual Mandelstam variables,

$$s = (p_1 + p_2)^2, \tag{1.43}$$

$$t = (p_1 - p_3)^2, \tag{1.44}$$

and

$$u = (p_1 - p_4)^2, \tag{1.45}$$

for the two-to-two process $p_1p_2 \to p_3p_4$. s is the center-of-mass energy squared. The other Mandelstam variables, t and u can be written

$$t = -2(\frac{s}{4} - m^2)(1 - \cos\theta), \tag{1.46}$$

and

$$u = -2(\frac{s}{4} - m^2)(1 + \cos\theta), \tag{1.47}$$

where θ is the scattering angle in the center-of-mass frame.

At large scattering angles, $\theta \approx \pi$, these kinematic variables are related through $s = -2t = -2u$. In fact, the matrix elements for scattering to large angles can be found to be in the ratio

$$M^2_{gg\to gg}/M^2_{gg\to q\bar{q}}/M^2_{qg\to qg}/M^2_{q_1q_2\to q_1q_2} = 30.4/0.14/5.4/2.2. \tag{1.48}$$

Qualitatively, larger cross sections correspond to shorter mean free paths. This means that there is a shorter time between interactions and ultimately a shorter equilibration time. From these large angle cross sections one can estimate an equilibration time for quarks and an equilibration time for gluons. From the values of the matrix elements at large angles alone, one sees that the gluon equilibration time is shorter.

However, one must also consider the small-angle cross sections. For massless quanta, gluons, small-angle scatterings, correspond to either $t \to 0$ or $u \to 0$, so the matrix elements are divergent, and thus the cross section is divergent as well. The small-angle cross section is finite in a plasma, however, because the gluons pick up a finite Debye screening mass [11].

Once the cross sections have been calculated, the equilibration time is estimated. It was found that for gluons the equilibration time is $\tau_g \approx 1/2$ fm/c, and for quarks the equilibration time is $\tau_q \approx 2$ fm/c. Entropy is produced early in the collision. Assuming that after the thermalization, the entropy per unit rapidity remains constant, the initial temperatures can be estimated. The initial gluon temperature for a Au-Au collision at RHIC is 500 MeV, and the initial quark temperature is 200 MeV (hence, hot glue). Since the gluons are initially at such a high temperature, an enhancement of open charm production could potentially occur due to the process $gg \to c\bar{c}$ [8].

Ten years later [6, 7], this proposed thermal enhancement was studied in detail. Shor calculated both the thermal open charm yield and the open charm yield due to hard parton scattering, with the intention of determining whether the enhanced thermal charm would be a significant background to the thermal dilepton spectrum. Both of the calculations utilized only lowest order parton level matrix elements. The calculations followed the standard perturbative QCD prescription of folding parton densities with parton level cross sections. In the thermal calculation the parton densities were taken to be Boltzman distributions

$$f(P) = e^{-\frac{P}{T}}, \tag{1.49}$$

where P is the parton momentum and T is the plasma temperature. This calculation was not done in the hot glue scenario. Quarks and gluons are assumed to be in thermal equilibrium from the equilibration time, taken to be 1 fm/c.

Shor performed the first calculation of the open charm cross section for a central heavy-ion collision. This work claimed that since, in hadronic collisions, charm production is a hard process, nucleus-nucleus collisions could be thought of as a superposition of nucleon-nucleon collisions. Based on the experimental measurement of the A-dependence of charm production cross sections in p-A collisions [12], $\sigma \propto A^{\alpha}$, with $\alpha \approx 0.76$. For central (impact parameter, $b \approx 0$) nucleus-nucleus collisions, the number of charm pairs produced per unit of rapidity

$$(\frac{dN_{cc}}{d\eta})_{AA} = \frac{A^{\alpha+1/3}}{\sigma_{pp}^{inelastic}}(\frac{d\sigma_{cc}}{d\eta})_{pp}, \tag{1.50}$$

where η is the spatial rapidity of the charm pair and $\sigma_{pp}^{inelastic}$ is the total inelastic hadronic cross section. The total inelastic cross section is about 50(100) mb at RHIC (LHC). In this calculation, the nuclear effects are introduced through a simple scaling of hadronic distributions. Since the calculation is only done to lowest order in α_s, a K-factor of 3 is included to take into account higher order perturbative contributions, in both the hard scattering cross section and the thermal cross section calculations.

At RHIC energy, the number of charm pairs per central collision per unit of spatial rapidity was found to be approximately 0.8. According to Shor, the thermal charm becomes comparable if the initial plasma temperature is at least 400 MeV. The number of charm quark pairs per unit spatial rapidity produced in the thermal system is a strong function of the initial plasma temperature. The number produced increases by almost 3 orders of magnitude when the initial temperature is increased from 400 MeV to 600 MeV.

In the hot glue scenario [9], the dependence on initial temperature is not as strong. As the initial temperature is increased from 400 MeV to 600 MeV, the number of charm pairs per unit of rapidity increases by only a factor of three. However, Shuryak's analysis reaches the same conclusion: the thermal charm will become comparable to the charm produced in hard scattering when the initial plasma temperature is around 400 MeV. The differences in the temperature dependence can be explained by the difference in the way they chose the initial conditions. Shor used a fixed equilibration time of 1 fm/c and allowed the initial temperature to vary. Shuryak used a fixed initial entropy, and varied the initial temperature and the time so that the entropy produced would remain constant. By varying the initial temperature and keeping the initial time fixed, Shor was actually allowing the entropy produced in a nucleus-nucleus collision to vary.

Another group had shown the potential for open charm enhancement related to the formation of a plasma [13]. In the time following the collision but prior to the partons reaching equilibrium, a source for charm quark production exists. In this preequilibrium phase, there are many semi-hard gluons, the so-called minijet gluons. Since the parton density is high after the initial collision, these few GeV gluons can rescatter and create $c\bar{c}$ pairs. Müller and Wang showed that the number density of charm pairs produced in this preequilibrium timeframe, by rescattering of minijets, increased with the thermalization time. This result suggests that open charm production can be a measure of the thermalization time for the plasma. Furthermore, their rough estimates show that the preequilibrium charm yield is of

the same order as the charm yield from the initial collision, and so it is potentially measurable. Also, the A-dependence of the preequilibrium charm production rate is expected to be $\propto A^2$, which is stronger than the A-dependence for the initial fusion. The number of gluons in a nucleus is proportional to A, and the gluons are distributed over a cross sectional area proportional to $A^{2/3}$. The production rate in a central collision will be proportional to the density squared times the cross sectional area, $A^{4/3}$. Any deviation from the $A^{4/3}$ behavior, due to the geometry of the central collision, would be a measure of the importance of this rescattering phase.

At this point a solid prediction for the charm yield, via hard parton scattering, in an ultra-relativistic heavy-ion collision was necessary. Our work improved Shor's calculation in two ways: newly available next-to-leading order matrix elements were utilized [14], and additional nuclear structure function data was incorporated [15]. This allowed a more accurate perturbative calculation of open charm production in heavy-ion collisions, which is detailed in chapters 2 and 3 [16]. Chapter 4 discusses the background to open charm production, open bottom production. Since both charm and bottom will be detected through their subsequent decays into dileptons, calculations of the invariant mass spectra of decays into dimuons is included. This calculation is detailed in chapter 6 [17]. Also, I have included the first next-to-leading order calculation of thermal heavy quark production in chapter 5.

Since my involvement in this project, other groups have performed similar calculations, most notably Gavai, et al. [18] and Lin/Gyulassy [19]. Their contributions to the field will be discussed and compared to our results in the conclusion.

1.4 Heavy-Ion Experiments

Some experimental groups intend to measure the open charm production in heavy-ion collisions. There are two proposed heavy-ion colliders where the search for the QGP seems quite promising. At Brookhaven National Laboratory, the Relativistic Heavy-Ion Collider (RHIC) will be capable of pp, pA and AA collisions at center-of-mass energies of 200 GeV/A. At CERN, the Large Hadron Collider (LHC) will be capable of colliding pp and AA at center-of-mass energies of 5.5 TeV/A.

1.4.1 PHENIX

One of the large experiments at RHIC, PHENIX plans to measure the charm production in Gold-Gold and proton-Gold collisions. This will be done by measuring electron-muon coincidences. It is difficult to separate the charm contribution to the dilepton mass spectrum using electrons or muons alone. By using a muon detector in the endcap and a central electron spectrometer, an unambiguous measurement of the $D\bar{D}$ cross section can be made. No correlated $e\mu$ pair can come from Drell-Yan or thermal production. By using like sign $e\mu$ coincidences to remove the background due to random semi-leptonic decays of pions and kaons, the $D\bar{D}$ cross section can be measured.

In the central region, a cut in the transverse momentum of the electron of $p_\perp > 1$ GeV will be implemented. Also, only muons with a momentum greater than 2 GeV will be accepted. These cutoffs minimize the background rates of electrons from Dalitz decays and of muons from weak pion and kaon decays. Even with these cutoffs, PHENIX will be able to measure $e\mu$ pairs in the mass range $1.5 < m_{e\mu} < 7$ GeV and rapidities near zero.

1.4.2 ALICE

At the LHC, A Large Ion Collider Experiment (ALICE) is planning on measuring the open charm produced in Lead-Lead collisions. Lower mass charmed hadrons can only decay through weak interactions. They travel a spatial distance of about 100 μm before decaying. The branching ratio for decays into all charged particles is large, so charmed hadrons can be directly detected via reconstruction of secondary vertices. An important parameter which quantifies the ability of a detector to separate secondary vertices is the impact parameter. The impact parameter is defined as the spatial distance between the reconstructed secondary vertex and the primary vertex. This is not the standard definition of impact parameter. Charm decays have an impact parameter of about 100 μm. ALICE will have an impact parameter resolution of 50 μm, so they will have sufficient precision to perform discrimination of secondary vertices

Neutral D mesons will be detected through the decay of a D-meson to a kaon and a pion. The expected signal-to-background ratio is $2 \cdot 10^{-5}$. By imposing a cut on the angle between the momentum of the D^0-candidate and the line connecting the primary and secondary vertices, the signal to background ratio can be improved. This angle should be zero for the signal and randomly distributed for the background. The signal to background ratio can be as high as 2 %. Since the branching ratio for charged D to a kaon is much larger the signal to background ratio for the charged D-meson is around 3 %.

CHAPTER 2

The Total Open Charm Cross Section in Hadronic and Heavy-Ion Collisions

Our calculation of open charm production cross sections in heavy-ion collisions is based on the formalism used in the calculation of heavy-quark production cross sections in hadronic collisions. With this we incorporate nuclear structure functions and nuclear geometry.

2.1 Hadronic Collisions

In perturbative QCD, the total inclusive cross section for charm production in hadronic collisions is obtained through a convolution of parton densities in the hadron with the hard scattering cross section. The calculation of the parton level scattering cross sections include both the leading order subprocesses, $O(\alpha_s^2)$, such as $q + \bar{q} \rightarrow Q + \bar{Q}$ and $g + g \rightarrow Q + \bar{Q}$, and next-to-leading order subprocesses, $O(\alpha_s^3)$, such as $q + \bar{q} \rightarrow Q + \bar{Q} + g$, $g + q \rightarrow Q + \bar{Q} + g$, $g + \bar{q} \rightarrow Q + \bar{Q} + \bar{q}$ and $g + g \rightarrow Q + \bar{Q} + g$. The calculations of the parton level cross sections are full NLO calculations, and as such both real and virtual gluon emission diagrams are included. In fact, when a soft light parton is emitted these matrix elements contain collinear and infrared divergences that are only canceled when the virtual gluon emission digrams are included.

The total inclusive cross section for charm production in hadronic collisions

can be written:

$$\sigma_c = \int_{\frac{4m_c^2}{s}}^1 dx_a \int_{\frac{4m_c^2}{x_a s}}^1 dx_b \sum_{i,j}^{partons} [F_i(x_a, Q^2) F_j(x_b, Q^2) \hat{\sigma}_{i,j}(\hat{s}, m_c^2, Q^2)], \tag{2.1}$$

where the $F_i(x, Q^2)$'s are the parton distributions in a nucleon, x_a and x_b are the fractional momenta of the incoming partons and $\hat{s} = x_a x_b s$ is the parton-parton center of mass energy. The parton-level cross section $\hat{\sigma}_{i,j}(\hat{s}, m_c^2, Q^2)$ has been calculated to the order $O(\alpha_s^3)$ and can be written as

$$\hat{\sigma}_{i,j}(\hat{s}, m_c^2, Q^2) = \frac{\alpha_s^2(Q^2)}{m_c^2} f_{i,j}(\rho, \frac{Q^2}{m_c^2}), \tag{2.2}$$

where

$$f_{i,j}(\rho, Q^2/m_c^2) = f_{i,j}^{(0)}(\rho) + 4\pi\alpha_s(Q^2)[f_{i,j}^{(1)}(\rho) + \bar{f}_{i,j}^{(1)}(\rho) \ln(Q^2/m_c^2)], \tag{2.3}$$

and

$$\rho = \frac{4m_c^2}{\hat{s}}, \tag{2.4}$$

and

$$\beta = \sqrt{1-\rho}. \tag{2.5}$$

The functions $f_{i,j}^{(0)}$, which determine the cross section to leading order, are given by

$$f_{q\bar{q}}^{(0)}(\rho) = \frac{\pi\beta\rho}{27}[2+\rho], \tag{2.6}$$

$$f_{gg}^{(0)} = \frac{\pi\beta\rho}{192}[\frac{1}{\beta}(\rho^2 + 16\rho + 16)\ln(\frac{1+\beta}{1-\beta}) - 28 - 31\rho], \tag{2.7}$$

$$f_{gq}^{(0)} = 0. \tag{2.8}$$

The NLO corrections, $f_{i,j}^{(1)}$ and $\bar{f}_{i,j}^{(1)}$, are given in Ref. [20]. The functions, $f^{(1)}$ depend on the scheme used for renormalization and factorization. These functions were calculated in an extension of the $\overline{MS}$ renormalization and factorization scheme [21]. To one-loop order the scheme is completely specified as follows. Graphs with a light parton loop use the usual $\overline{MS}$ subtraction scheme for renormalization. The two-point function of the heavy quark field, $\Gamma^{(2)}(p, m)$, obeys the following renormalization conditions:

$$\Gamma^{(2)}(p, m)|_{p^2=m^2} = 0, \tag{2.9}$$

which means that the mass, m, corresponds to a pole in the renormalized propagator; and

$$\frac{d}{d\not{p}}\Gamma^{(2)}(p,m)|_{p^2=0} = 1, \tag{2.10}$$

which fixes the heavy quark field wave function renormalization. From these conditions, both the mass renormalization and the heavy quark field renormalization have anomalous dimension equal to zero. The Taylor-Slavnov identity fixes the $gQ\bar{Q}$ vertex renormalization. The treatment of divergent graphs with heavy quark external lines is specified completely. Graphs containing heavy quark loops are subtracted at zero momentum. In this scheme the heavy quarks are decoupled at low energy [22], so the light partons obey the same renormalization group that they do in the absence of heavy quarks. The NLO running coupling constant and two-loop $\bar{M}S$ evolved structure functions should be used.

The running of the coupling constant is determined by the renormalization group. The coupling constant $\alpha_s(Q^2)$, calculated to next-to-leading order, is given by

$$\alpha_s(Q^2) = \frac{12\pi}{(33-2N_f)\ln\frac{Q^2}{\Lambda^2}}[1 - \frac{6(153-19N_f)\ln\ln Q^2/\Lambda^2}{(33-2N_f)^2\ln Q^2/\Lambda^2}], \tag{2.11}$$

where Q^2 is the renormalization scale, Λ is the QCD scale parameter and N_f is the number of flavors. We take the factorization scale in the structure functions to be $2m_c$ and we consider the renormalization scales $Q = m_c$ and $Q = 2m_c$. For the mass of the charm quark we use $m_c = 1.5$GeV. We do not consider the factorization scale below $2m_c$ because the structure functions have been measured only for $Q^2 \geq 8.5$GeV [23]. In our calculation we use two-loop-evolved parton structure functions:

1) Martin, Roberts and Stirling, MRS S0 [24], with $\lambda_5 = 140$ MeV.

2) Martin, Roberts and Stirling, MRS D0 [24], with $\lambda_5 = 140$ MeV.

3) Martin, Roberts and Stirling, MRS D– [24], with $\lambda_5 = 140$ MeV and "singular" behavior of the gluon distribution at small x, i.e. $G(x,Q^2) \sim x^{-1.5}$.

4) Martin, Roberts and Stirling, MRS A [25], with $\lambda_5 = 151$ MeV and "singular" behavior of the gluon distribution at small x, i.e. $G(x,Q^2) \sim x^{-1.08}$. This was the most recent MRS set, adjusted to fit recent H1 and ZEUS data [23].

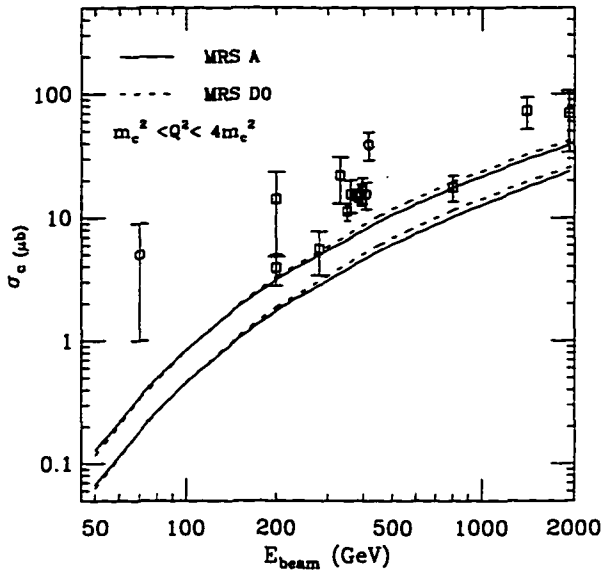

Figure 2.1: The total cross section for charm quark production in proton-proton collisions calculated to the next-to-leading order (LO+NLO) for values of E_{beam} ranging from 50 GeV to 2 TeV for two renormalization scales, $Q = m_c$ and $2m_c$. The lower curves correspond to $Q = 2m_c$ and the upper curves correspond to $Q = m$. The results are compared to the data for $p-p$ and $p-A$ collisions [26].

In Fig. 2.1, I present our results for the total cross section for charm production in proton-proton collisions for the beam energies ranging from 50 GeV up to 2 TeV. The results were obtained using two different sets of structure functions, MRS D0 (dashed lines) and MRS A (solid lines). We find the uncertainty due to the choice of structure function to be only few percent. This is not surprising, because the range of x probed by charm quark pair production at these energies is well within the range of the data for nucleon structure functions. The top two curves in Fig. 2.1 correspond to the calculation using the renormalization scale $Q^2 = m_c^2$ and the bottom two to $Q^2 = 4m_c^2$. Comparison of my results with low energy data for p-p and p-A collisions [26] indicate better agreement for the choice of

the renormalization scale $Q^2 = m_c^2$. Even lower values for Q, $Q = \frac{m_c}{2}$ for instance, may provide even better agreement with the low energy data. However, due to the low mass of the charm quark, this choice of renormalization scale would be too close to Λ to permit a reliable perturbative calculation. Future high-precision charm experiments at Fermilab [27] might be able to provide a tighter constraint on this theoretical parameter.

We find that the contribution from higher-order corrections, $(O(\alpha_s^3))$, are important at low energies, especially near the threshold energy for charm production. The K-factor, defined as a ratio of the next-to-leading order result to the leading-order one, ranges from about 3.7 at $E_{beam} = 50\text{GeV}$ to about 2.2 at $E_{beam} = 2\text{TeV}$.

We predict that the total cross section for charm production in p-p collisions is $180\mu b - 210\mu b$ (for $Q^2 = m_c^2$) and $112\mu b - 126\mu b$ (for $Q^2 = 4m_c^2$) at RHIC and $2.4mb - 15.3mb$ (for $Q^2 = m_c^2$) and $1.4mb - 9.2mb$ (for $Q^2 = 4m_c^2$) at LHC. The range of the cross sections is due to the choice of structure functions. At RHIC energies, the cross section depends weakly on the choice of the structure function. The average x-value that is probed with charm production at $\sqrt{s} = 200\text{GeV}$ is on the order of 10^{-2}, still within the range of x for which there is deep inelastic scattering data. Theoretical uncertainty due to the choice of the structure function is about 15%. At LHC energies ($\sqrt{s} = 7$ TeV) the average x-value probed with charm production in the central rapidity region is about 5×10^{-6}, far below the x-range covered by the current deep inelastic scattering data. Different sets of structure functions [24, 25], which all fit the current data have different extrapolations to the low-x region. The most recent H1 and ZEUS data on structure functions at low-x and low-Q^2 [23] are best fitted with MRS A distributions. The data seem to be steeper functions of x than the MRS D0 structure functions and not as steep as the MRS D- [24, 25]. For example, the MRS D- and MRS A gluon distribution have singular behavior in the small-x region, in contrast to MRS D0 and MRS S0 sets. As a consequence, the total cross section for charm production at LHC

calculated with MRS D– parton distributions is larger than the one obtained with MRS D0 set by about a factor of 6. The K-factor for the total cross section for charm production is between 2 and 2.1 at RHIC and between 2.3 and 2.8 at LHC. The range for the K-factor corresponds to the choice of the renormalization scale.

2.2 Charm Production in Nuclear Collisions

2.2.1 Nuclear Geometry

Assuming the validity of factorization theorems in the calculation of the cross section for charm production in nuclear collisions, the total number of charm quark pairs produced in A-A collisions at some fixed impact parameter is given by [28]

$$N_c^{AA}(s,b) = \int d^2b_1 dx_a dx_b \sum_{i,j}^{partons} [F_i^A(x_a, Q^2, |\vec{b} - \vec{b_1}|) F_j^A(x_b, Q^2, |\vec{b_1}|) \hat{\sigma}_{i,j}(\hat{s}, m_c^2)], \tag{2.12}$$

where the $F_i^A(x, Q^2, b)$ is the parton distribution function in a nucleus. We assume that the parton density in a nucleus can be factorized in terms of the (usual) parton structure function modified by the effects of the nuclear medium, $F_i^A(x, Q^2)/A$, and the spatial distribution of partons at some impact parameter b, $T_A(b)$, i.e.

$$F_i^A(x, Q^2, b) \approx (F_i^A(x, Q^2)/A) T_A(b). \tag{2.13}$$

The nuclear thickness function, $T_A(b)$, is the number of nucleons per unit transverse area at fixed impact parameter. The spatial (impact parameter) integration that appears in Eq. 2.12 gives the number of nucleon-nucleon collisions per unit of transverse area at fixed impact parameter, $T_{AA}(b)$, which is related to the nuclear density in the following way [29]:

$$T_{AA}(b) = \int d^2b_1 T_A(|\vec{b_1}|) T_A(|\vec{b} - \vec{b_1}|), \tag{2.14}$$

where the nuclear thickness function, $T_A(b)$, is the nuclear density integrated over the longitudinal size, i.e.

$$T_A(b) = \int_{-\infty}^{\infty} dz \rho_A(\sqrt{b^2 + z^2}). \tag{2.15}$$

For A-A collisions we take the nuclear density to be the Woods-Saxon distribution [30] given by

$$\rho(r) = \frac{n_0}{[1 + e^{(r-R_A)/d}]}, \tag{2.16}$$

where $n_0 \approx 0.17/\text{fm}^3$, R_A is the nuclear radius and $d = .54\text{fm}$ is the "skin" thickness of this distribution. The density and the nuclear overlapping function are normalized so that $\int d^3r\rho(r) = A$ and $\int d^2bT_{AA}(b) = A^2$. For central collisions the overlapping function can be approximated by $T_{AA}(0) = A^2/\pi {R_A}^2$, which gives $T_{Au-Au}(0) = 30.7\text{mb}^{-1}$.

The nuclear density that is most widely used in the literature is the Gaussian distribution

$$\rho(r) = \frac{A}{\pi^{3/2}a^3} e^{-r^2/a^2}, \tag{2.17}$$

where a is related to the charge radius of the nucleus, $\frac{3}{2}a^2 = \langle R_A^2 \rangle$. Functions $T_A(b)$ and $T_{AA}(b)$ can be obtained analytically and are given by

$$T_A(b) = \frac{A}{\pi a^2} e^{-\frac{b^2}{a^2}} \tag{2.18}$$

and

$$T_{AA}(b) = \frac{A^2}{2\pi a^2} e^{-\frac{b^2}{2a^2}}. \tag{2.19}$$

The formalism for proton-nucleus collisions is similar. The thickness function of the proton is approximated by

$$T_p(b) \simeq \frac{1}{(2\pi)^2} \int d^2k_\perp G_E(k_\perp^2) e^{i\mathbf{k}_\perp \cdot \mathbf{b}}, \tag{2.20}$$

where G_E is the proton electric form factor

$$G_E(k_\perp) \simeq (1 + \frac{k_\perp^2}{\nu^2})^{-2}. \tag{2.21}$$

The corresponding overlapping function is given by [31]

$$T_{pA}(b) = \frac{\nu^2 A}{48\pi a^2} \int_0^\infty db' b' e^{-(b^2+b'^2)/a^2} (\mu b')^3 K_3(\mu b') I_0(\frac{2bb'}{a^2}), \qquad (2.22)$$

where $\nu^2 \simeq 0.71(\mathrm{GeV})^2$. The expression for T_{pA} derived from a Woods-Saxon distribution cannot be obtained analytically. In Fig. 2.2. I present $T_{p-Au}(b)$ and $T_{Au-Au}(b)$ obtained with the Woods-Saxon and with the Gaussian nuclear density distributions. Although the Gaussian distribution is widely used, the corresponding overlapping function has a long tail and at high energies gives a total inelastic cross section that violates unitarity (i.e. the cross section is larger than the size of the physical system).

2.2.2 The Nuclear Shadowing Effect

Calculation of the charm production in nuclear collisions requires knowledge of the nucleon structure function *in-medium*, $F_i^A(x, Q^2)/A$, introduced in Eq. 2.13. If nucleons were independent parton densities in a nucleus, $F_i^A(x, Q^2)$, would be simply given as A times the parton density in a nucleon. However, at high energies, the parton densities become so large that the sea quarks and gluons overlap spatially and the nucleus can not be viewed as a collection of uncorrelated nucleons. This happens when the longitudinal size of the parton, in the infinite momentum frame of the nucleus, becomes larger than the size of the nucleon. Partons from different nucleons start to interact and through annihilation effectively reduce the parton density in a nucleus. When partons inside the nucleus completely overlap, they reach a saturation point. Motivated by this simple parton picture of the nuclear shadowing effect and taking into account the $A^{1/3}$ dependence obtained by considering the modified, nonlinear Altarelli-Parisi equations with gluon recombination included, the modifying factor to the parton structure function in a nucleus can

be written as [32]

$$R(x,A) \equiv \frac{F_i^A(x,Q^2)}{AF_i^N(x,Q^2)} = \begin{cases} 1-\frac{3}{16}x+\frac{3}{80} & .2 < x \leq 1 \\ 1 & x_n < x \leq .2 \\ 1-D(A^{1/3}-1)\frac{1/x-1/x_n}{1/x_A-1/x_n} & x_A \leq x \leq x_n \\ 1-D(A^{1/3}-1) & 0 < x < x_A \end{cases} \tag{2.23}$$

where $F_i^N(x,Q^2)$ is the parton structure function in a nucleon, x_n is the value of x which specifies the onset of the shadowing effect ($x_n = 1/(2r_p m_p) \approx 0.1$), x_A corresponds to the saturation point ($x_A = 1/(2R_A m_p)$), m_p is the mass of the proton, r_p is the radius of a proton and R_A is the radius of the nucleus. It is important to note that x_n is fixed for *all* nuclei, and x_A can be determined for each nucleus. Thus, the only parameter that is free to be fitted is D. In Fig. 2.3, $R(x,A)$, given by Eq. 2.23, is plotted by fitting D to deep inelastic lepton-nucleus data on the ratio $F_2^A(x,Q^2)/F_2^D(x,Q^2)$ [15]. $R(x,A)$ has a much steeper x-dependence than the data, especially for $0.002 \leq x \leq 0.1$, the region of relevance to charm production at RHIC and LHC energies. Even the best fit overestimates the observed shadowing effect by about 15%. Consequently charm production calculated with this shadowing function would be underestimated by about 40%.

At low energies, the effect from shadowing ranges from 3% at E_{beam} = 50GeV to 6% at E_{beam} = 2 TeV in p-Au collisions and from 6% at E_{beam} = 50GeV to 13% at E_{beam} = 2 TeV in Au-Au collisions. This effect is even smaller for a lighter nucleus. The nuclear shadowing effect is so small since the x-region probed by charm production at these energies is $0.05 \leq x \leq 1$, not too far from the value for the onset of shadowing, $x_n \approx 0.1$.

Recently, a new parametrization of the nuclear shadowing function given by [33]

$$R(x,A) = \begin{cases} \alpha_3 - \alpha_4 x & x_0 < x \leq 0.6 \\ (\alpha_3 - \alpha_4 x_0)\frac{1+k_q\alpha_2(1/x-1/x_0)}{1+k_q A^{\alpha_1}(1/x-1/x_0)} & x \leq x_0 \end{cases} \tag{2.24}$$

has been proposed. This new function gives a much better description of all EMC, NMC and E665 data [15] than the shadowing function of Eq. 2.23. This is illustrated in Fig. 2.3. The parameters k_q, α_1, α_2, α_3 and x_0 are fitted to deep-inelastic data for the ratio $F_2^A(x,Q^2)/F_2^D(x,Q^2)$ [15] and can be found in [33]. In our calculation of charm production in p-Au and Au-Au collisions we use the nuclear shadowing function given by Eq. 2.24.

Presently there is no theory which can quantitatively describe the observed nuclear shadowing effect [15]. Recent calculations of the perturbative gluon shadowing seem to substantially underestimate the observed effect, indicating perhaps that the non-perturbative effects are large and can not be neglected [34]. Better understanding of the nuclear shadowing effect might require a novel, non-perturbative approach.

To obtain the effective A-dependence of the total inclusive charm cross section in nuclear collisions, defined as $\sigma_c^{AA} = A^{\alpha_{eff}}\sigma_c^{pp}$, we use the total charm cross section in hadronic collisions at $\sqrt{s} = 200$GeV ($\sqrt{s} = 7$TeV) to be $\sigma_c^{pp} = 180\mu$b ($\sigma_c^{pp} = 2.4$mb). The corresponding α_{eff} for central (inelastic) Au-Au collisions is 1.27 (1.94) at RHIC and 1.2 (1.87) at the LHC.

To be able to determine the fraction of central or inelastic events which contain at least one charm quark pair, consider the semiclassical probability of having at least one parton-parton collision at fixed impact parameter, $1 - e^{-N_c(b)}$, where $e^{-N_c(b)}$ is the probability that there is *no* parton-parton scattering in a Au-Au collision at impact parameter b. The fraction of events in Au-Au collisions that contain at least one charm quark pair is then given by

$$\frac{\sigma_c^{AA}}{\sigma_{inelastic}^{AA}} = \frac{\int d^2b[1 - \exp(-N_c(b))]}{\int d^2b[1 - \exp(-T_{AA}(b)\sigma_{in}^{pp})]}, \tag{2.25}$$

where N_c is given by Eq. 2.12.

To determine the fraction of all *central* events that contain at least one charm quark pair integrate Eq. 2.25 over a small range of impact parameter, i.e.

$0 \leq b \leq 0.1 fm$. We find that 98% (99%) of central events at RHIC (LHC) energies will contain at least one charm quark pair. For *inelastic* collisions, integrate Eq. 2.25 over all impact parameters. We find this fraction to be 38% at RHIC and ranging from 54% to 72% at the LHC. Note that the integrated charm cross section in Eq. 2.25 includes multiple independent parton-parton scatterings which means multiple charm quark pair production.

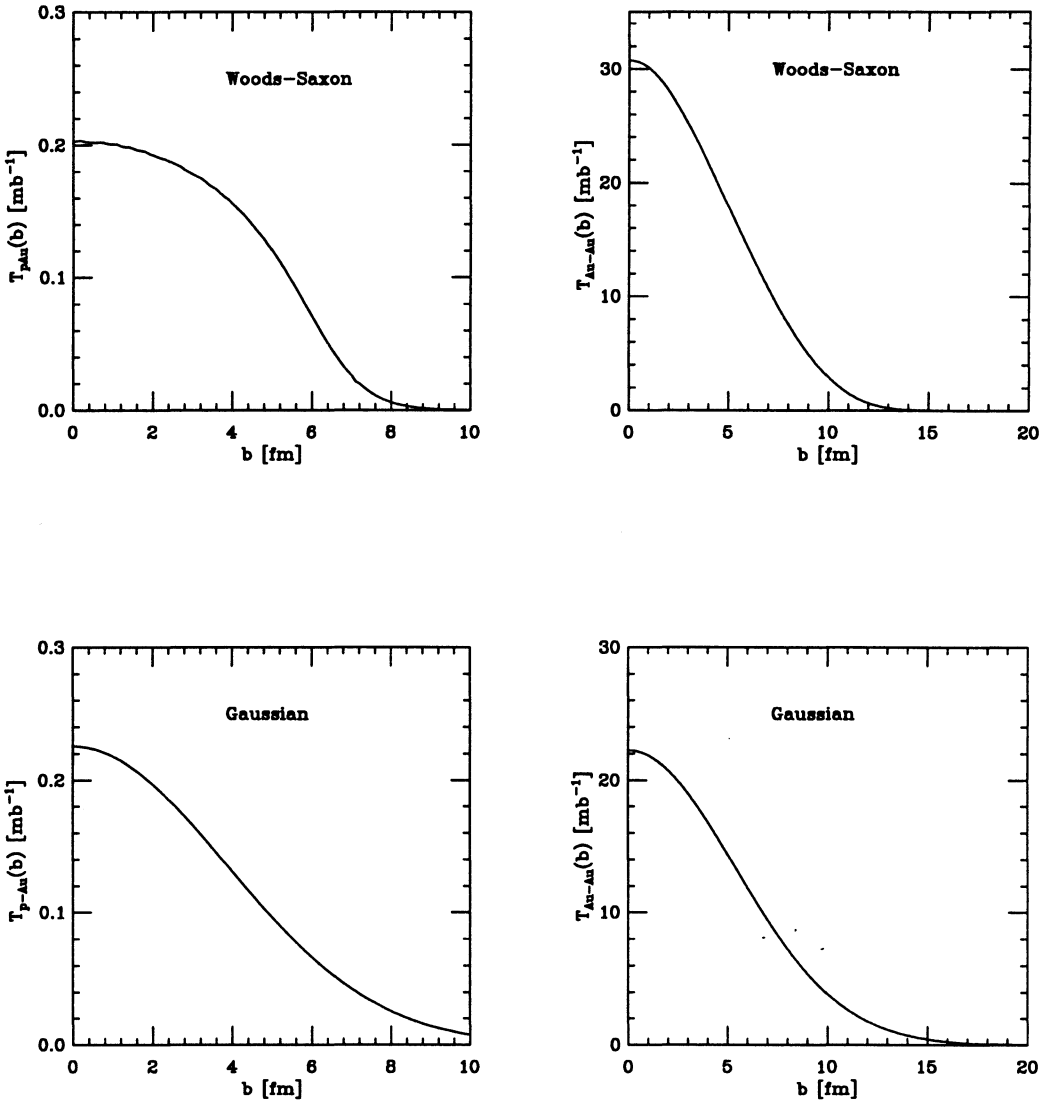

Figure 2.2: The nuclear overlapping functions, $T_{AB}(b)$ for p-Au and Au-Au collisions obtained with two different nuclear density functions, a) Woods-Saxon [30] and b) the Gaussian form.

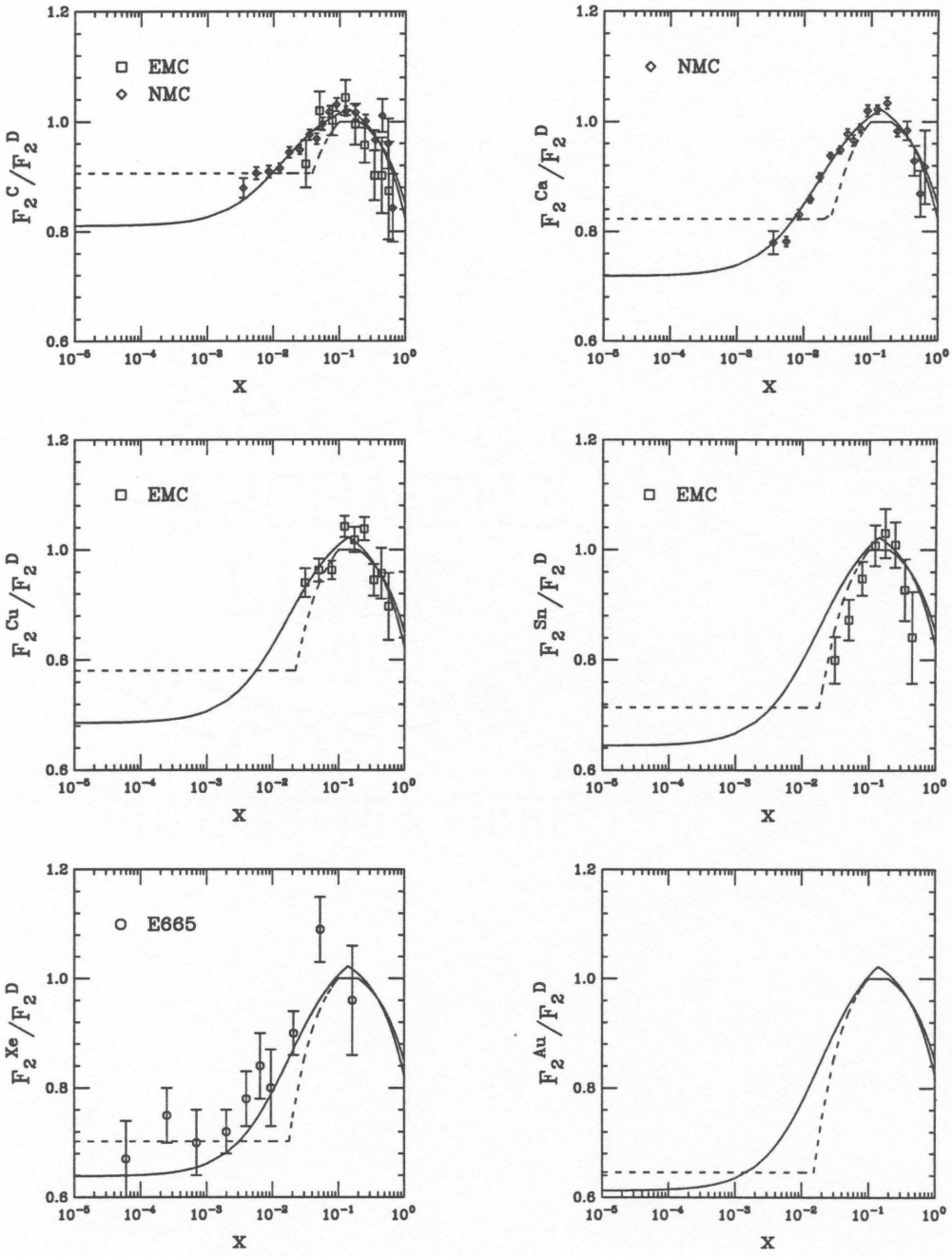

Figure 2.3: The nuclear shadowing functions given by Eq. 2.24 (solid line) and by Eq. 2.23 (dashed line) fitted to the EMC, NMC and E665 deep-inelastic lepton-nucleus data [15]. I include a plot of the nuclear shadowing function for Au given by Eq. 2.24 (solid line), which is used in our calculation of charm production in p-Au and Au-Au collisions.

CHAPTER 3

The Rapidity and Transverse Momentum Distributions for Open Charm Production in Hadronic and Heavy-Ion Collisions

Experimentally, it is very difficult to measure a total cross section. An experiment would need a full 4π steradians coverage. However, measurements can be made in different regions of phase space. The differential cross sections more readily lend themselves to comparison with experiment.

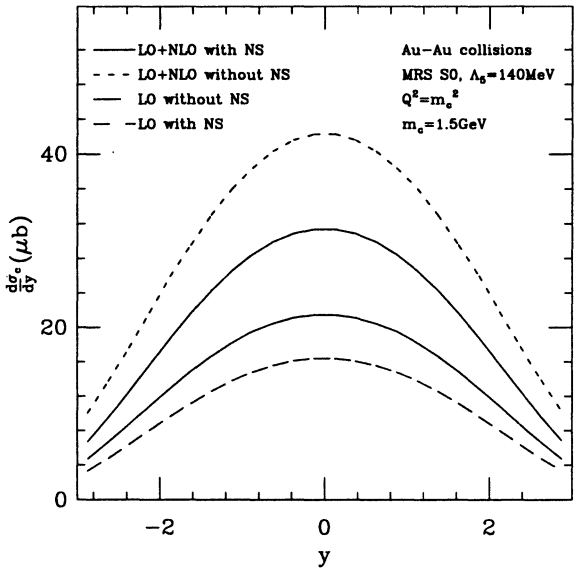

Figure 3.1: Rapidity distributions of inclusive charm quark production in Au-Au collisions at RHIC, calculated to next-to-leading order including nuclear shadowing (NS) (solid line), without NS (dotted line), only leading-order (LO) without NS (long-dashed line), and with NS (short-dashed line)

In the previous chapter I have shown that the nuclear shadowing function

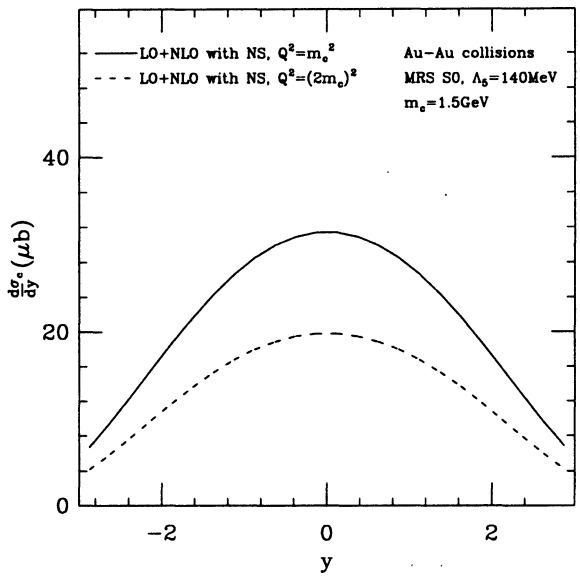

Figure 3.2: Rapidity distributions of inclusive charm quark production at RHIC, but for two different choices of the scale, $Q^2 = m_c^2$ (solid line) and $Q^2 = 4m_c^2$ (dotted line)

depends on the kinematic variable, x. Thus, it seems plausible that the effect that nuclear shadowing has on charm production is not uniform throughout all of phase space. Furthermore, the new subprocesses that are part of the next-to-leading order calculation have different contributions in different regions of phase space. By studying the single differential distributions one might be able to get more information about the underlying dynamics of charm production in nuclear collisions.

In general, the single differential distribution is obtained by integrating the double differential inclusive distribution

$$\frac{dN_c}{d^2p_T dy} = T_{AA}(0)\frac{d\sigma_c}{d^2p_T dy}, \tag{3.1}$$

where the double differential inclusive cross section per nucleon-nucleon interaction

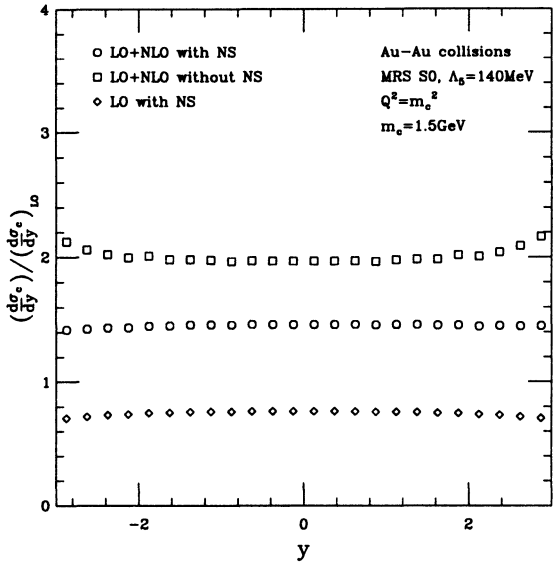

Figure 3.3: The *effective* K-factor, $K \equiv (\frac{d\sigma_c}{dy})/(\frac{d\sigma_c}{dy})_{LO}$, for the distributions presented in Fig. 3.1 The K-factor for the next-to-leading order distribution without NS (squares), including NS (circles) and for the leading-order (LO) distribution with NS (diamonds). Note that $K \approx 2$ for hadronic (proton-proton) collisions (squares).

in-medium is given by

$$\frac{d\sigma_c}{d^2p_T dy} = \sum_{i,j}^{partons} \int dx_a dx_b \frac{F_i^A(x_a, Q^2)}{A} \frac{F_j^A(x_b, Q^2)}{A} \frac{d\hat{\sigma}_{i,j}(Q^2, m_c, \hat{s})}{d^2p_T dy}. \tag{3.2}$$

Heavy quark production in hard parton-parton scatterings can be described in the following kinematic framework: let the incoming light parton four-momenta be given by k_1 and k_2, the heavy quark four-momenta be given by p_1 and p_2 and the four-momentum of the radiated light parton be given by p. The center-of-mass energy squared at the parton level is given by the Mandelstam variable

$$\hat{s} = (k_1 + k_2)^2. \tag{3.3}$$

The "hat" distinguishes the parton-level kinematic variables from the hadronic-level kinematic variables. The energy enters the cross section formulae through

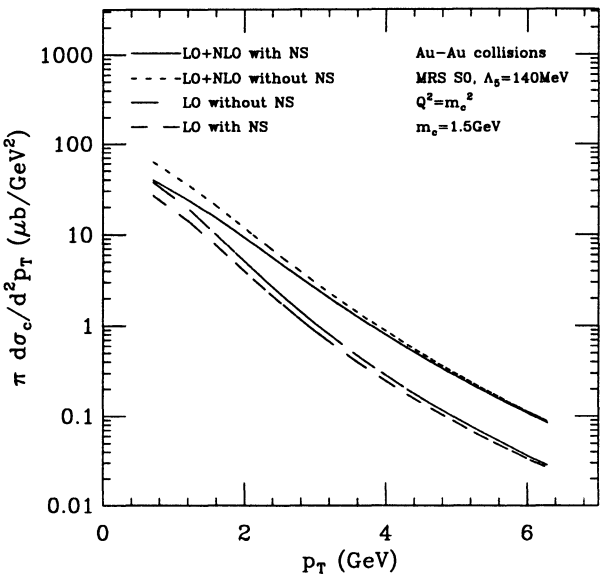

Figure 3.4: The transverse momentum distributions of inclusive charm quark production at RHIC. Curves are labeled as in Fig. 3.1.

the variable

$$\hat{\rho} = \frac{4m_c}{\hat{s}}. \tag{3.4}$$

The dependence of the heavy quark cross section on the opening angle of the heavy quark is expressed in terms of the variables

$$\tau_i = \frac{p_1 \cdot k_i}{k_1 \cdot k_2}, i = 1, 2. \tag{3.5}$$

In a $2 \rightarrow 2$ process, τ_1 is related to τ_2. The sum

$$\tau_1 + \tau_2 = \frac{1}{k_1 \cdot k_2}(p_1 \cdot k_1 + p_1 \cdot k_2), \tag{3.6}$$

$$= \frac{1}{k_1 \cdot k_2}(p_1 \cdot (k_1 + k_2)). \tag{3.7}$$

By energy-momentum conservation

$$\tau_1 + \tau_2 = \frac{1}{k_1 \cdot k_2}(p_1 \cdot (p_1 + p_2)). \tag{3.8}$$

The center-of-mass energy squared, $\hat{s}$, in terms of the initial four-momenta, is

$$\hat{s} = 2k_1 \cdot k_2, \tag{3.9}$$

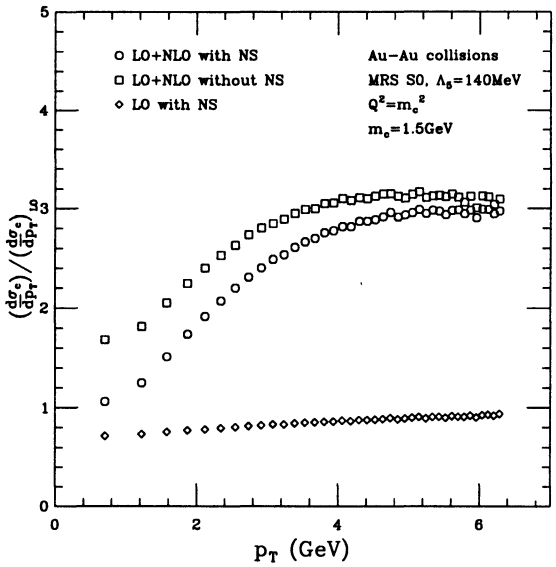

Figure 3.5: The *effective* K-factor for the transverse momentum distributions presented in Fig. 3.4. Labeling is the same as in Fig. 3.3.

and in terms of the final state four-momenta, is

$$\hat{s} = 2m_c^2 + 2p_1 \cdot p_2. \tag{3.10}$$

Therefore,

$$\tau_1 + \tau_2 = 1. \tag{3.11}$$

For this reason, the variable

$$\tau_x = 1 - \tau_1 - \tau_2 \tag{3.12}$$

is also important. For nonzero τ_x, the process is a $2 \rightarrow 3$ process. As $\tau_x \rightarrow 0$, the emitted light parton is soft.

The parton differential cross section calculated to $O(\alpha_s^3)$ can be written [14]

$$\frac{d\hat{\sigma}_{i,j}}{d^2p_T dy} = \frac{\alpha_s^2}{\hat{s}} H_{i,j}^{(0)} + \frac{\alpha_s^3}{2\pi\hat{s}^2} H_{i,j}^{(1)}. \tag{3.13}$$

The leading order, $O(\alpha_s^2)$, contribution to the cross section is written in terms of

$$H_{ij}^{(0)} = h_{ij}^{(0)}(\tau_1, \rho)\delta(\tau_x), \tag{3.14}$$

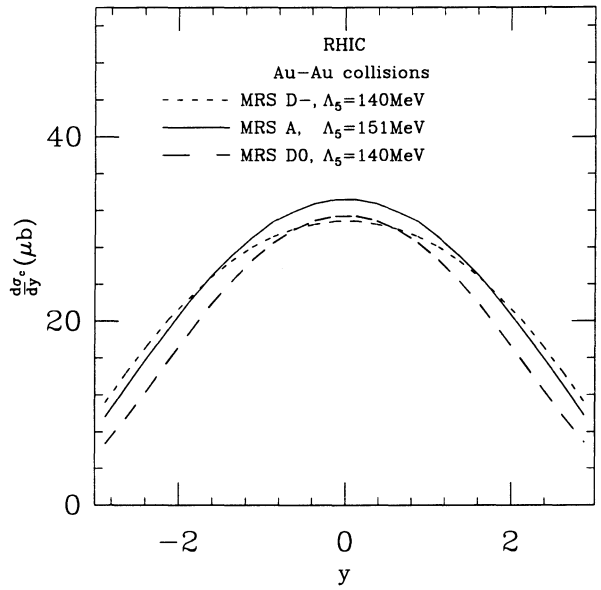

Figure 3.6: The rapidity distribution for charm quark production in Au-Au collisions at RHIC energies calculated to $O(\alpha_s^3)$ with three different sets of structure functions: MRS A (solid line), MRS D– (dotted line), and MRS D0 (dashed line). The renormalization scale is taken to be $Q = m_c$.

where

$$h_{gg}^{(0)} = \frac{2T_f}{D_A}\left(\frac{C_f}{\tau_1\tau_2} - C_A\right)\left(\tau_1^2 + \tau_2^2 + \rho - \frac{\rho^2}{4\tau_1\tau_2}\right) \tag{3.15}$$

for the $2 \rightarrow 2$ gluon fusion processes, and

$$h_{q\bar{q}}^{(0)} = \frac{c_f^2}{D_A}(2\tau_1^2 + 2\tau_2^2 + \rho) \tag{3.16}$$

for the $2 \rightarrow 2$ quark-anti-quark annihilation processes, with, for color SU(3), $C_A = 3$, $C_f = 4/3$, $T_f = 1/2$, and $D_A = 8$. Thus, $H^{(0)}$ is everywhere regular. There are no surprises in the leading order calculation.

The next-to-leading order, $O(\alpha_s^3)$, cross section formulae are not so simple. They can be expressed:

$$\begin{aligned} H_{ij}^{(1)} &= (h_{ij}^{(d)}(\tau_1,\rho) + \xi\bar{h}_{ij}^{(d)}(\tau_1,\rho))\delta(\tau_x) \\ &\quad +(h_{ij}^{(+)}(\tau_1,\tau_2,\rho) + \xi\bar{h}_{ij}^{(+)}(\tau_1,\tau_2,\rho))[\frac{1}{\tau_x}]_+ \end{aligned}$$

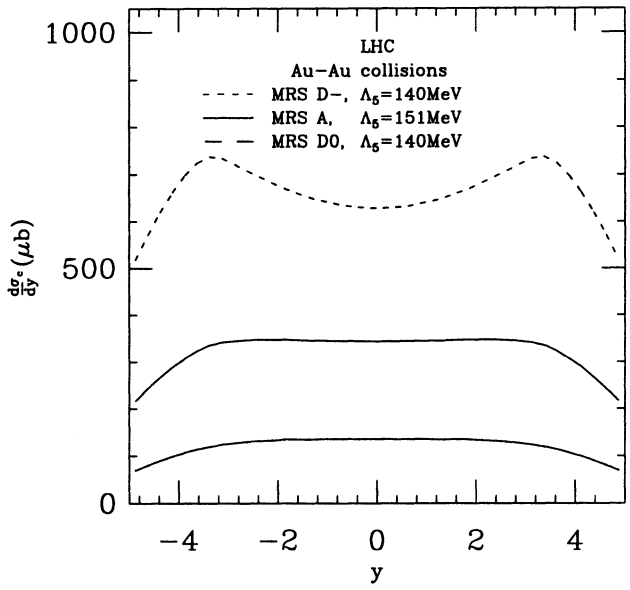

Figure 3.7: The rapidity distributions for charm quark production at LHC for three different structure functions. The curves are labeled as in Fig. 3.6.

$$+h_{ij}^{(1)}(\tau_1,\tau_2,\rho)[\frac{\log(\tau_x)}{\tau_x}]_+, \tag{3.17}$$

where ξ holds the dependence on the subtraction scale for the collinear and ultraviolet divergences, μ,

$$\xi = \ln(\frac{\mu^2}{m_c^2}). \tag{3.18}$$

The terms proportional to $\delta(\tau_x)$ in 3.17 appear due to the inclusion of diagrams which represent the emission and reabsorption of virtual gluons. There are counter events, which arise from the virtual diagrams and the collinear subtraction. In this factorization scheme, one uses the "+ function" prescription to cancel the collinear singularities in the initial state radiation. These "+ functions" are defined

$$\int_0^1 d\tau_x f(\tau_x)[\frac{1}{\tau_x}]_+ = \int_0^1 d\tau_x \frac{f(\tau_x)-f(0)}{\tau_x}, \tag{3.19}$$

and

$$\int_0^1 d\tau_x f(\tau_x)[\frac{\log(\tau_x)}{\tau_x}]_+ = \int_0^1 d\tau_x (f(\tau_x)-f(0))\frac{\log(\tau_x)}{\tau_x}. \tag{3.20}$$

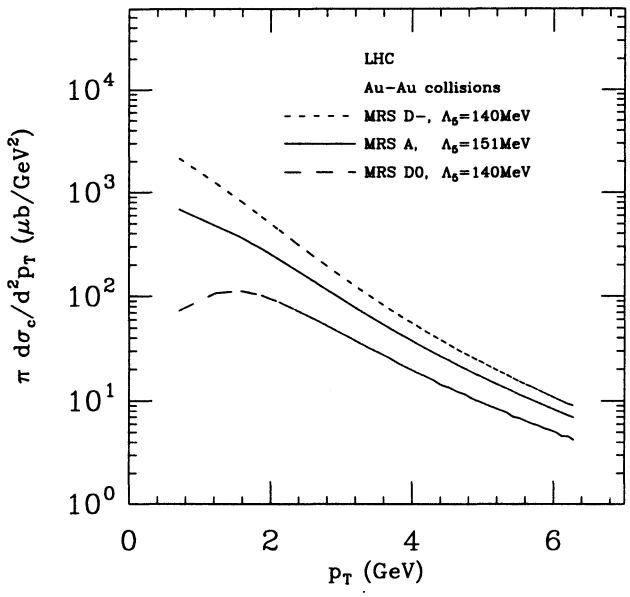

Figure 3.8: The rapidity distributions for charm production at LHC for three different structure functions. The curves are labeled as in Fig. 3.6.

In fact, since we are dealing with the case of heavy quark production, these cross sections are infrared safe quantities because the heavy quark mass acts as a cutoff for final state collinear singularities. Thus, the heavy quark mass sets the scale for a perturbative expansion in the strong coupling constant.

3.1 Summary of Charm Production Results

The rapidity and transverse momentum distribution for charm production in p-p, p-Au and Au-Au collisions were obtained by integrating Eq. 3.2 over the appropriate variable (i.e. to obtain the rapidity distribution, for example, integrate Eq. 3.2 over the transverse momentum). Two different choices of the renormalization scale are used, as in the case of the total cross section, and three different structure functions: MRS D0, MRS D– and MRS A [24, 25].

The result for the rapidity distribution of inclusive charm production in

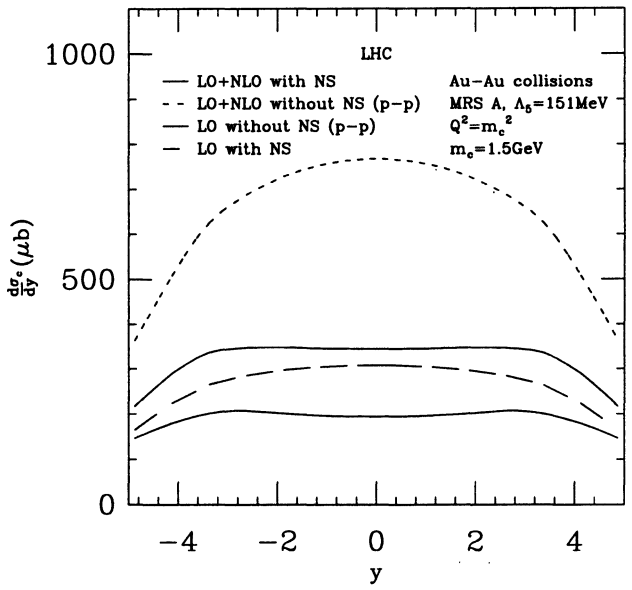

Figure 3.9: The rapidity distribution for charm quark production in proton-proton and Au-Au collisions at LHC energies calculated to the next-to-leading order, The labeling is the same as in Fig. 3.1

central Au-Au collisions at RHIC is presented in Fig. 3.1 (solid line), as well as the rapidity distribution when nuclear shadowing is not included (dotted line) and the leading-order results with shadowing (short-dashed line) and without shadowing (long-dashed line). Note that the *shape* of the rapidity distribution does not seem to be affected by the next-to-leading corrections or by the nuclear shadowing effect. In Fig. 3.2 the results for two different choices of scale are presented, illustrating the uncertainty due to this particular choice. In the central rapidity region, the number of charm quark pairs produced per unit rapidity in central Au-Au collisions at RHIC is 0.6 for the scale $Q = 2m_c$ and 0.9 for the scale $Q = m_c$.

In hadronic collisions, one usually defines the "K-factor" as a measure of the size of higher-order corrections. The *effective* K-factor for *nuclear* collisions is defined as a ratio of the particular distribution to the leading-order distribution without any nuclear effects. Fig. 3.3 presents the results for the K-factor. In hadronic collisions the K-factor is about 2 (squares), while the *nuclear* K-factor

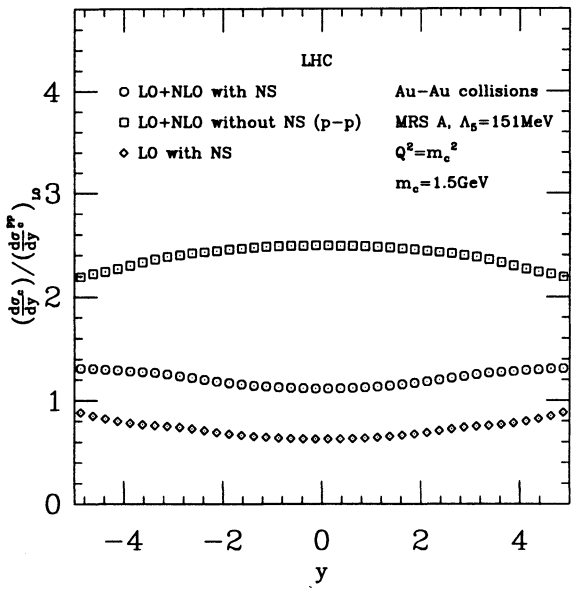

Figure 3.10: The *effective* (in-medium) K-factor for the distributions in Fig. 3.9. The K-factor for p-p collisions is about 2.5 (squares), while the K-factor *in-medium* (in case of Au-Au collisions) is about 1.1 (circles) in the central rapidity region.

is about 1.4 (circles) in the central rapidity region ($|y| \leq 3$). This is due to the fact that the nuclear shadowing effect effectively suppresses production of charm quarks by about 30%.

In Fig. 3.4, I present the results for the transverse momentum distribution of the charm quark produced in Au-Au collisions at RHIC (solid line). Both the higher-order correlations and the nuclear effects change the shape of p_T distribution. The nuclear shadowing effect is much stronger at low p_T (about 40% effect), while at $p_T = 6$GeV it reduces the cross section by only few percent. The next-to-leading order corrections give a factor of 1.7 increase at low p_T and about factor of 3 at $p_T = 6$GeV. These two effects together result in effective K-factor increasing from 1 at $p_T = 1$GeV to 3 at $p_T = 6$GeV. At large p_T, where nuclear shadowing effects are negligible, the K-factor is expected to approach its hadronic value.

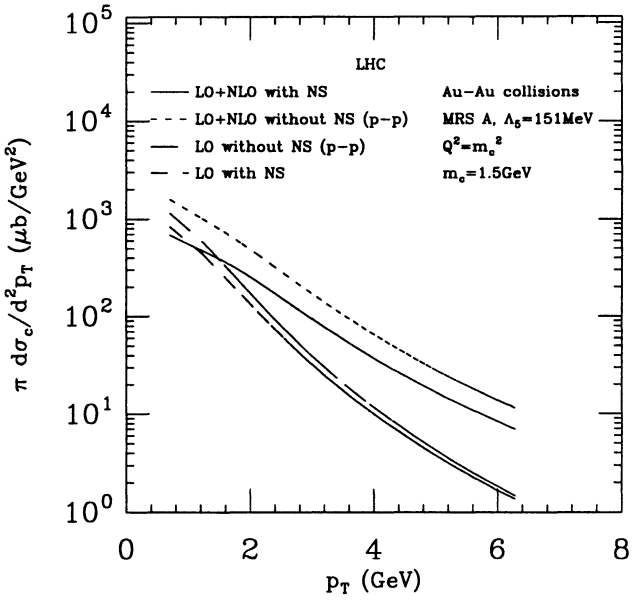

Figure 3.11: The transverse momentum distribution for charm production at LHC. Curves are labeled as in Fig. 3.1.

In Fig. 3.6, the results for the rapidity distribution for charm production at RHIC are presented. The use of different structure functions result in about 8% uncertainty at y=0, while at $y = 3$ this uncertainty is almost 40%. This is due to the fact that charm production in the large rapidity region is probing the smaller x-region than in the case where charm quarks are produced in the central rapidity region ($x_{average} \approx 0.01$ for $y \approx 0$ and $x_{average} \approx 10^{-5}$ for $y \approx 3$). At LHC energies, the choice of the structure functions introduces a much larger theoretical uncertainty. From Fig. 3.7, note that at $y \approx 3$ this uncertainty is about a factor of 7. Furthermore, the shape of the rapidity distribution is sensitive to the low-x behavior of the structure function, resulting in a "dip" at $y = 0$. At $y = 0$, the x-values of the incoming partons are approximately 10^{-4}, and therefore both of the structure functions that appear in the distribution given by Eq. 3.2 are evaluated in the region of maximum nuclear shadowing. When $y \approx 3.5$, the x-region probed is a combination of small-x (maximum shadowing) and intermediate-x (small shadowing effect) leading to the larger values for the number of charm

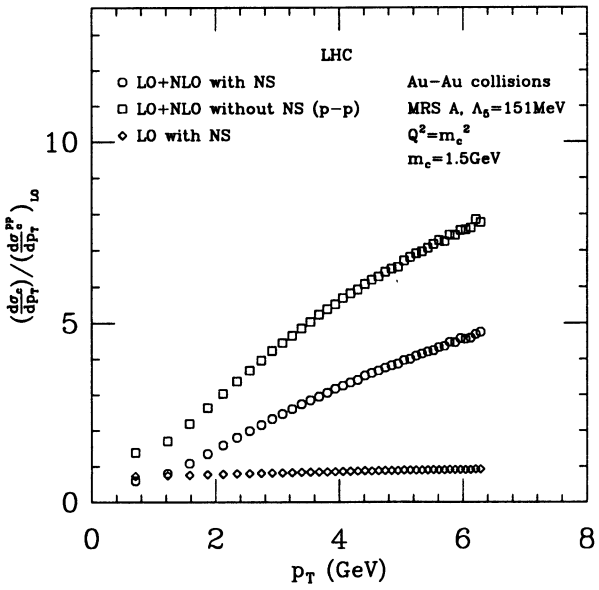

Figure 3.12: The K-factors for the distributions in Fig. 3.11. The labeling is the same as in Fig. 3.3. The K-factor for p-p collisions ranges from 1.4 at $p_T = 0.7$ GeV to 7.6 at $p_T = 6$ GeV. In the same p_T range, the K-factor *in-medium* increases from 0.6 to 4.6.

quarks produced than in the central rapidity region. Furthermore, the combination of the x-dependence of the nuclear shadowing effect and the steep increase of the structure function at low-x could result in less overall shadowing at $y \approx 3.5$. In Fig. 3.7, note that this is apparent for the MRS D– structure function, while the effect is much smaller in case of MRS A and MRS D0 sets. In Fig. 3.8, I present the results for the transverse momentum distributions for the charm production at LHC. The shape of the p_T distribution is sensitive to the choice of the structure function. The p_T distribution is much steeper when obtained with MRS D– structure function than with MRS A or with MRS D0 set. The theoretical uncertainty due to the choice of the structure function is about an order of magnitude at low p_T, where the small-x region is probed, while at larger values of p_T (i.e. $p_T \geq 6$GeV) this uncertainty is substantially reduced. In Fig. 3.9, I present the rapidity distribution for charm production at LHC energies calculated

with the MRS A parton distribution and with $Q^2 = m_c^2$. The two distributions without nuclear shadowing correspond to p-p collisions. To obtain the number of charm quark pairs produced in Au-Au collisions, multiply the rapidity distribution which contains the nuclear shadowing effect (solid line) with the geometrical factor (i.e. the spatial, overlapping function) presented in Fig. 2.2. To get the number of charm quark pairs produced in central collisions (i.e. at zero impact parameter), for example, one would need to multiply $d\sigma_c/dy$ by $T_{AA}(0)$. Note that the rapidity distribution for charm production in Au-Au collisions at LHC obtained with the MRS A structure function is flat for $|y| \leq 3$.

The *effective* (in-medium) K-factor can be defined in a way analogous to the hadronic K-factor, namely as the ratio of a particular distribution for charm production in *nuclear* collisions to the leading-order distribution without any nuclear effects. Thus, this K-factor is a measure of the size of the effect due to higher-order corrections *combined* with nuclear effects. In Fig. 3.10, I present the K-factor for the rapidity distributions at LHC energies. Over the range $-5 \leq y \leq 5$, the K-factor has a weak dependence on y. In the central rapidity region, the K-factor for Au-Au collisions is about 1.1 (circles), while the hadronic K-factor is 2.5 (squares).

In Fig. 3.11, I present results for the transverse momentum distributions at the LHC. The calculation is done using MRS A parton distributions and a renormalization scale $Q^2 = m_c^2$. At low-p_T the nuclear shadowing effects suppress charm production by about 62%, while the higher-order corrections, $O(\alpha_s^3)$, enhance the charm production by about 50%, resulting in p_T distributions which are effectively lower than the leading-order result for p-p collisions. From Fig. 2.3, note that the nuclear shadowing of a parton distribution in gold at $x \leq 10^{-4}$ is about 62%. From Eq. 3.2, the production rate includes the product of two density functions, the overall suppression will be about 62% at low-p_T. At large p_T, nuclear effects are expected to become negligible and so the p_T distribution will approach the next-to-leading order results for p-p collisions. In Fig. 3.12, I present the hadronic and the *effective* K-factor for the transverse momentum distribution for charm

production at LHC energies. While the hadronic K-factor varies from 1.4 to 7.6 for 0.7 GeV$\leq p_T \leq$ 6 GeV, the K-factor for Au-Au collisions changes from 0.6 to 4.6 in the same p_T range. For the x_F-distribution, the *effective* K-factor for Au-Au collisions at RHIC (LHC) energies increases from 1.5 (1.2) at $x_F \approx 0$, to around 5.2 (3) at $x_F \approx 1$, while the hadronic K-factor changes from 2 (2.4) at $x_F \approx 0$, to about 6.6 (5) at $x_F \approx 1$.

The results for the single differential distribution in p-A collisions can be expressed in terms of the parameter α_{eff}, defined as

$$\tilde{\sigma}_{AA} = A^{\alpha_{eff}} \tilde{\sigma}_{pp}, \tag{3.21}$$

where $\tilde{\sigma}_{pp}$ is a differential cross section for charm production in hadronic collisions, and $\tilde{\sigma}_{AA}$ is the corresponding cross section in nuclear collisions. The parameter α_{eff} is a sum of the geometrical contribution and the nuclear shadowing effect (i.e. $\alpha_{eff} = \alpha + \alpha_{NS}$, $\alpha_{NS} < 0$). The later effect reduces the value of the "standard" α, which for minimum bias A-A collisions is 2, while for the central A-A collisions, $\alpha = 4/3$. The values for $\alpha_{NS} \equiv \alpha_{eff} - \alpha$ in p-A and A-A collisions at RHIC and LHC are presented in Fig. 3.13. Knowing $\alpha_{eff}(y)$ and $\alpha_{eff}(p_T)$ it is possible to extract the rapidity and the transverse momentum distribution for p-A collisions by suitable modification of the distribution for charm production in p-p collisions. For example, $\frac{d\sigma_c^{pA}}{dy} = A^{\alpha_{eff}(y)} \frac{d\sigma_c^{pp}}{dy}$. The K-factor for inclusive distribution for charm production in p-A collisions can also be determined from α_{eff}, as $K = (\frac{d\sigma_c^{pA}}{dy})/(\frac{d\sigma_c^{pp}}{dy})_{LO}$.

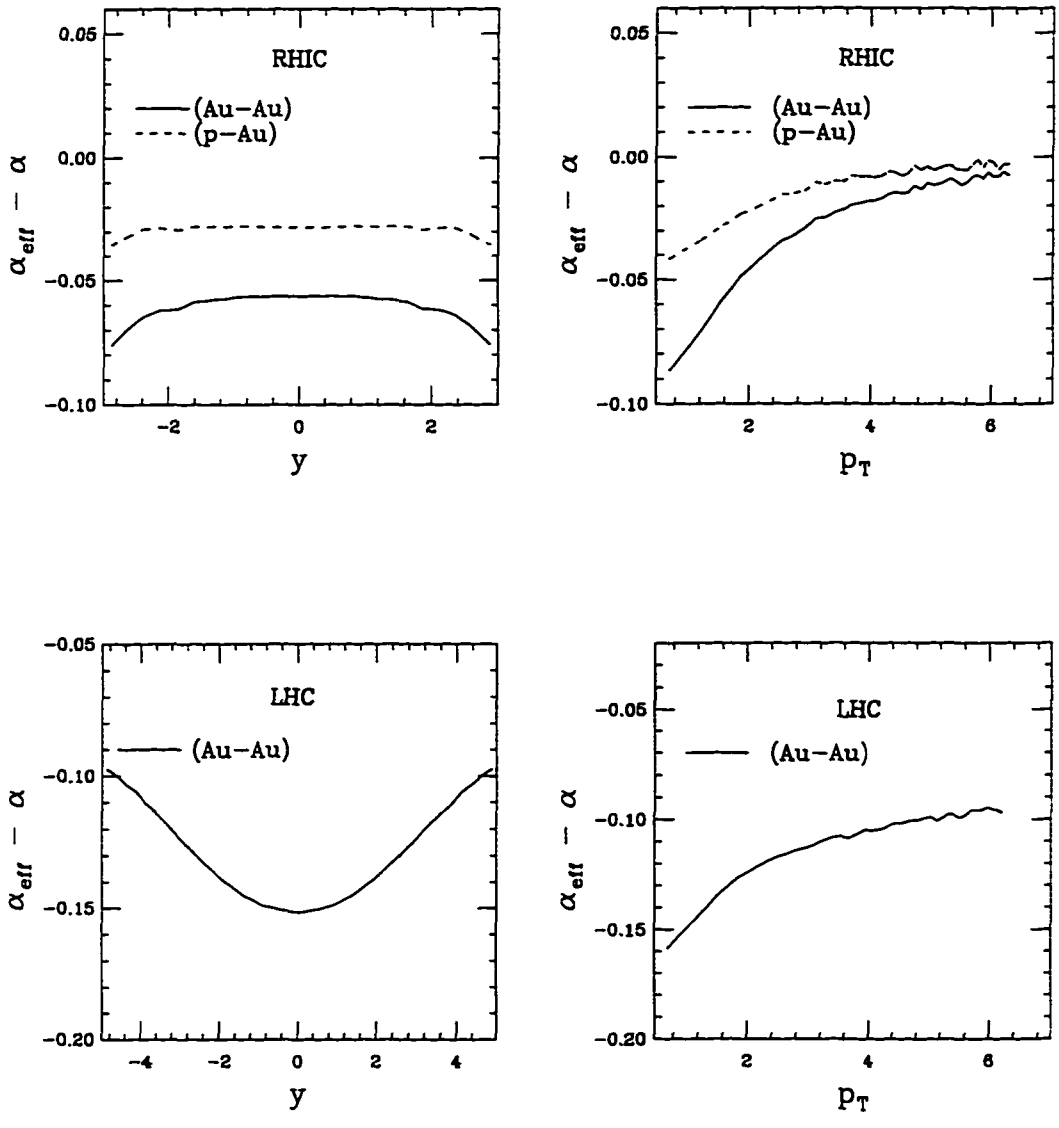

Figure 3.13: The plot of $\alpha_{eff} - \alpha$ as a function of y and p_T for p-Au and Au-Au collisions.

CHAPTER 4

Open Bottom Production in Hadronic and Heavy-Ion Collisions

Future hadronic and heavy-ion experiments at RHIC and LHC, PHENIX (RHIC), ALICE (LHC), and CMS (LHC), are currently being planned to measure the open charm production. The PHENIX experiment will be looking for dilepton coincidences as a signature for charm production in the central rapidity region ($y \approx 0$) and at higher rapidity ($y \approx 2$). ALICE will have full acceptance in the central rapidity region, $|\eta| < .9$. The CMS is planning on full muon detection up to $|\eta| = 2.4$. Each of these groups has expressed interest in our work, and has asked

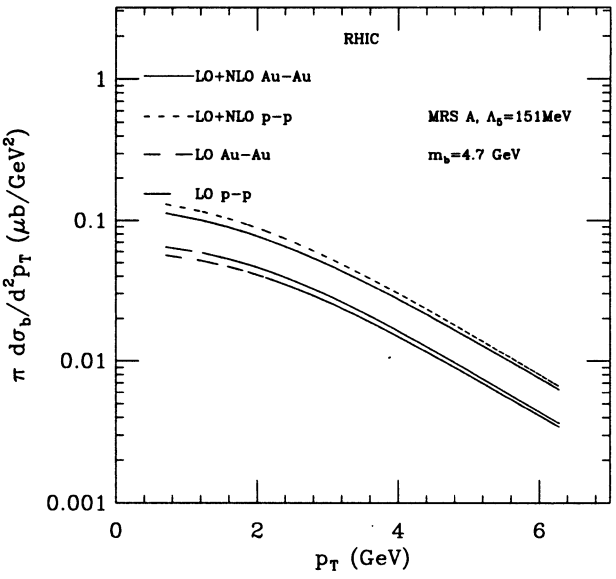

Figure 4.1: The transverse momentum distribution for bottom production at RHIC. The curves are labeled as in Fig. 3.1

us to provide information on the background processes. One of the signatures

for charm production is di-muon coincidences. The primary background for this process is $B\bar{B} \rightarrow \mu^+\mu^-$, so it is important to compare the bottom production to the charm prediction. Since the mass of the bottom quark is large compared to the QCD scale, we expect perturbative QCD calculations to be even more reliable than in the case of charm. We have calculated rapidity and p_T distributions for bottom quark production in p-p and Au-Au collisions at RHIC and LHC energies.

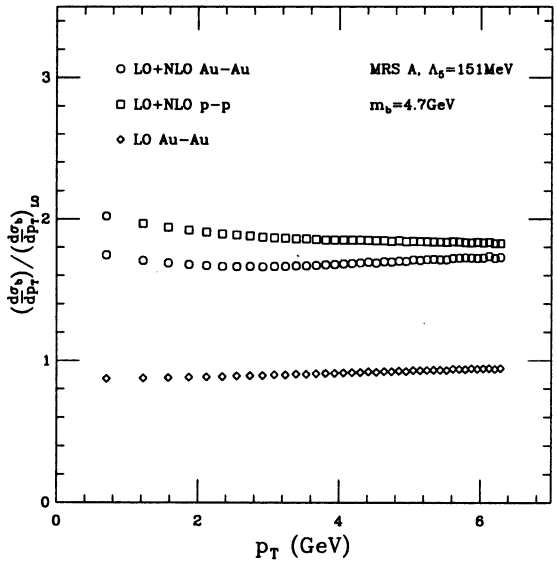

Figure 4.2: The effective K-factor for the transverse momentum distribution for bottom production at RHIC.

In our calculations we have taken the bottom quark mass to be m_b = 4.7GeV. Both the factorization and renormalization scales were taken to be μ = m_T,the transverse mass. All of the calculations were performed using the MRS A [25] structure function. The uncertainty due to the choice of structure function was found to be 10% at RHIC and 17% at LHC. At RHIC(LHC) energies the number of bottom quark pairs produced per unit rapidity in central Au-Au collision in the central rapidity region is 0.01 (0.4), while the total number is .04 (3.3). The *effective* (nuclear) K-factor for the total bottom cross section at RHIC (LHC) is

1.7 (1.3), reflecting significant shadowing at LHC energies only.

At RHIC energies, the NLO terms enhance the cross section for bottom production by a factor of 2 at low transverse momentum ($p_T \approx .7$GeV), but the NLO terms only enhance the cross section by a factor of 1.82 at higher transverse momentum ($p_T \approx 6$GeV). The nuclear shadowing effect suppresses the cross section by 13% at low transverse momentum and 6% at high transverse momentum. In this range, .7GeV$< p_T <$ 6GeV, the *effective* K-factor is roughly constant and has the value 1.73, as can be seen in Fig. 4.2.

In the rapidity distributions of bottom quark production at RHIC energy, the higher order perturbative corrections enhance the central rapidity region by a factor of 1.8 and at $y = 3$ by a factor of 2.4. The shadowing correction suppresses

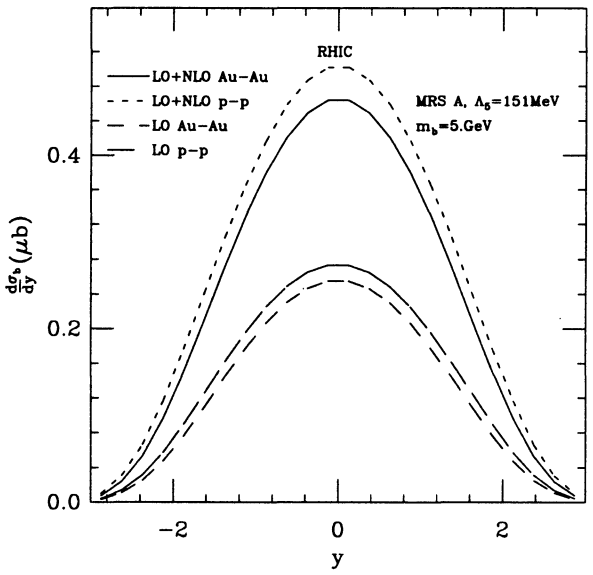

Figure 4.3: The rapidity distribution for bottom production at RHIC.

the cross section in the central rapidity region by 7 % and at $y = 3$ it suppresses the bottom production by 25 %. The overall effect can be seen in Fig. 4.4. The *effective* K-factor has a weak dependence on y. In the range, $-3 < y < 3$, the value of this K-factor is between 1.7 and 1.8.

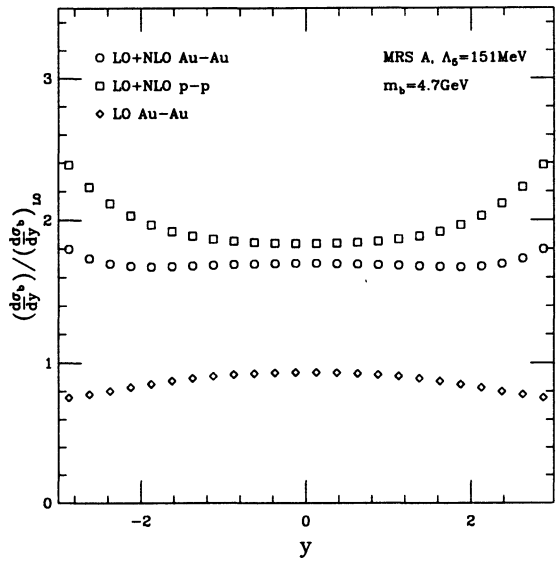

Figure 4.4: The effective K-factor for the rapidity distribution for bottom production at RHIC.

AT LHC energies, the NLO perturbative corrections have a considerable transverse momentum dependence. At low $p_T(\approx .7\text{GeV})$, the higher order terms enhance the cross section by a factor of 2.1. At higher transverse momentum, $p_T \approx$ 6GeV, there is a factor of 2.6 enhancement of the cross section. The K-factor due to the higher order corrections increases by 20% over the range .7GeV$< p_T <$ 6GeV. At LHC energies, the shadowing corrections become quite large. Over this range of transverse momentum, the shadowing correction suppresses the distribution almost uniformly by 47%. The *effective* K-factor for bottom production in Au-Au collisions has a transverse momentum dependence. From Fig. 4.6, the K-factor varies from 1.1 to 1.5.

The K-factors depend only weakly on rapidity. In the central rapidity region the higher order corrections enhance the cross section by a factor of 2.4 and the shadowing suppresses the cross section by 47% for an overall factor of 1.2 enhancement, as can be seen in Fig. 4.8.

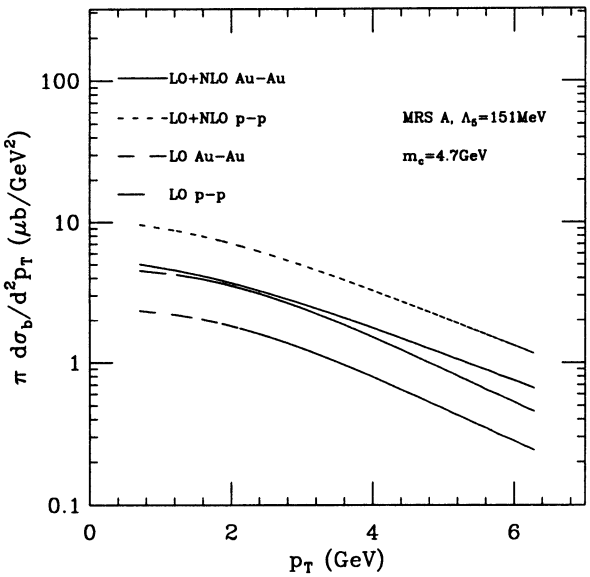

Figure 4.5: The transverse momentum distribution for bottom production at LHC.

The total number of bottom pairs produced in a central Au-Au collision at RHIC (LHC) is .04 (3.3), whereas there are 4 (110) charm pairs produced. It would seem that bottom production is not an important background for charm production. However, because of the large bottom mass, dilepton pairs from bottom decays tend to have larger invariant masses. In the invariant mass spectrum of the dileptons there will be a region where the dileptons from the bottom decays will overtake the dileptons produced from the charm decays.

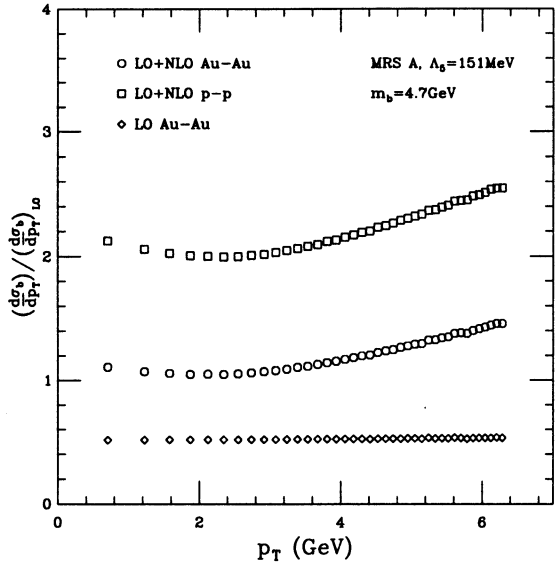

Figure 4.6: The effective K-factor for the transverse momentum distribution for bottom production at LHC.

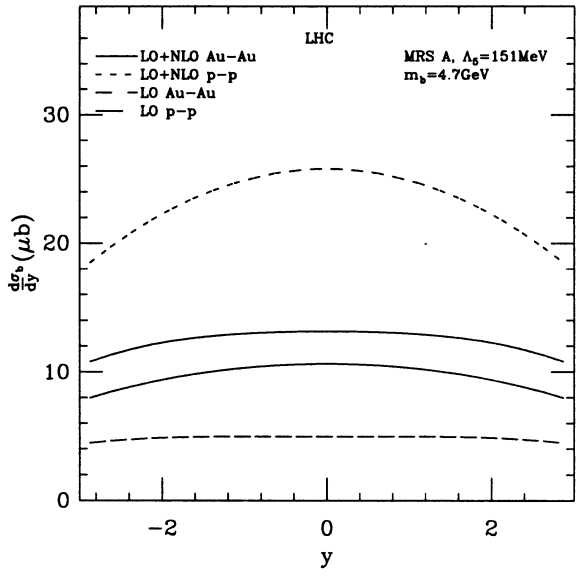

Figure 4.7: The rapidity distribution for bottom production at LHC.

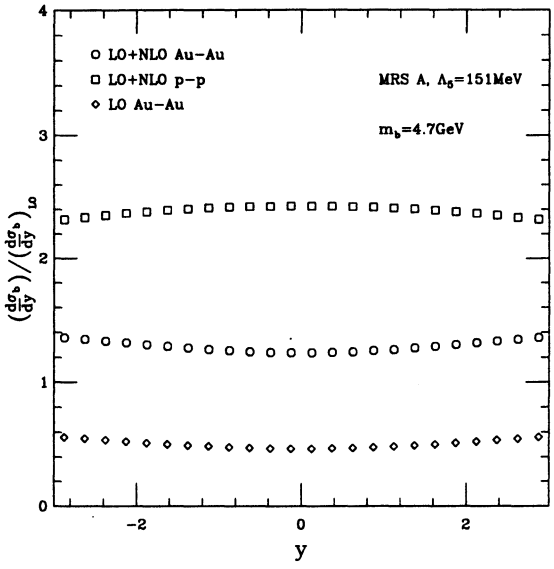

Figure 4.8: The effective K-factor for the rapidity distribution for bottom production at LHC.

CHAPTER 5

Thermal Production of Open Heavy Flavors

In order to ground the discussion of thermal charm production, recall Bjorken's supposition [1] about the space-time evolution after a high-energy heavy-ion collision. Immediately after the collision of two nuclei, the energy density at the space-time point of impact can be very high, a few GeV/fm^3. Quark matter with this energy density will be in the QGP phase and not the hadronic phase. The hard parton scatterings in a nucleus-nucleus collision occur on a very short time scale, and the dense parton gas created in the wake of the heavy-ion collision is not immediately in thermal and chemical equilibrium. The created parton gas will expand and approach thermal equilibrium via the free streaming of its partons. It was estimated for RHIC energies [35] that at proper time, $\tau_0 = .7$ fm/c, after the collision there is a local isotropy of parton momenta. This time is assumed to be the time that it takes for the parton gas to come into thermal equilibrium. The gas continues to expand after thermal equilibrium is reached. As the gas expands, it cools. Eventually, the average kinetic energy (temperature) will fall below some critical value, T_c. At this point, there will be a phase transition to the hadronic phase. It is still unknown whether this is a first or second order phase transition.

At sufficiently high temperatures, a thermal system of light partons can create a charm pair. The thermal charm production has been calculated so far at the leading order matrix element level [19, 36]. To estimate the reliability of the leading order result, one has to perform a full NLO calculation. At the next-to-leading order, there are additional $2 \rightarrow 3$ processes and loop diagrams. Formally, the differential production rate is given by the convolution of the parton

level differential cross sections with the initial light parton phase space densities (distribution functions) $f_i(p)$ (we neglect the final state Fermi blocking or Bose-Einstein enhancement)

$$E\frac{dR}{d^3p} = \int \frac{d^3k_1}{(2\pi)^3 2E_1}\frac{d^3k_2}{(2\pi)^3 2E_2}F(k_1,k_2)\left[\frac{g_{gg}}{2}f_g(k_1)f_g(k_2)E\frac{d\hat{\sigma}_{gg}}{d^3p}+ g_{q\bar{q}}f_q(k_1)f_{\bar{q}}(k_2)E\frac{d\hat{\sigma}_{q\bar{q}}}{d^3p}+g_{qg}f_q(k_1)f_g(k_2)E\frac{d\hat{\sigma}_{qg}}{d^3p}\right], \tag{5.1}$$

where $g_{gg} = 16^2$, $g_{q\bar{q}} = 6^2N_f$ and $g_{qg} = 6\cdot 16N_f$ are the degeneracy factors, and $F(k_1,k_2) = 4k_1k_2$ is the inverse flux factor. The parton densities were taken to be Boltzman distributions. We assume that these distributions are boost invariant,

$$f_i(k) = e^{-\beta k_\perp \cosh(y-\eta)}, \tag{5.2}$$

where β is $1/T$ and η is the spatial rapidity,

$$\eta = \frac{1}{2}\ln\frac{(t+z)}{(t-z)}. \tag{5.3}$$

By integrating 5.1 over spacetime, d^4x, one obtains the number of thermal charm pairs produced in d^3p. The parton level cross sections are the same as those in Chapter 3.

At the leading order, the $d\hat{\sigma}_{qg}$ term is absent. At the next-to-leading order, these parton level differential cross sections contain $2 \rightarrow 3$ processes and loop diagrams and they are not infrared finite quantities. Braaten and Pisarski [37] have shown that a resummation technique has to be employed to take into account the so-called "hard thermal loops" which give the same order of magnitude contributions as the leading order terms when the external momenta of the amplitude are soft. As a result of the resummation, the infrared singularities are shielded by a Debye screening effect, and the screening masses of gluons and quarks provide an infrared cutoff. The perturbative resummation can only regularize the electric part of the propagators and so far the magnetic screening mass has to come from the unknown nonperturbative effect. As a qualitative calculation, the Debye screening

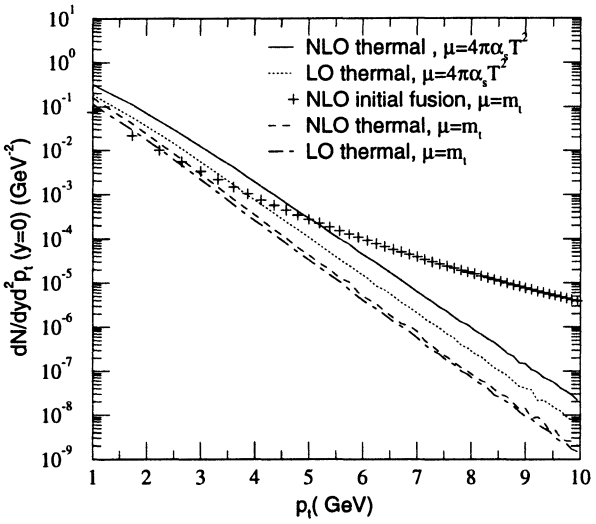

Figure 5.1: The charm differential distribution produced in an ideal thermalized quark-gluon plasma at the leading and the next-to-leading orders in perturbative QCD. The sensitivity on the choice of the scale is illustrated. The charm production at the NLO from the initial hard scattering is also plotted for comparison.

mass [38]

$$\mu_D^2 = \frac{6g^2}{\pi^2}\int pf(p)dp = 4\pi\alpha_s T^2 \,, \tag{5.4}$$

is used to regularize all singularities in the radiative cross sections. This amounts to a "massive gluon scheme" where the μ_D^2 sets the scale for the parton level cross sections in Eq.(5.1). Certainly, this calculation is not entirely consistent, and the results thus obtained can only be taken as a qualitative indication of the reliability of the leading order result. The thermal charm yield has been evaluated at RHIC energy by integrating over the space-time evolution of the quark-gluon plasma. We assume a fully equilibrated thermal system with an initial temperature $T_0 = 0.55$ GeV and a Bjorken ideal fluid scaling $T(\tau)/T_0 = (\tau_0/\tau)^{1/3}$ with $\tau_0 = 0.7$ fm/c and $T_c = 0.2$ GeV. A spatial rapidity cutoff $\eta_{\max} = 3$ is assumed. The differential distributions are plotted in Fig. 5.1 for the leading order and the next-to-leading order calculations using the Debye screening scale in (5.4). We also compare the result for a choice of the scale $\mu = m_t$. As in the initial hard scattering case, the

higher order corrections are sizable with an effective K-factor, $K \sim 2$.

CHAPTER 6

The Dilepton Mass Spectrum from Heavy Quark Decay

The emission of dileptons in high energy heavy-ion collisions provides an excellent probe of the property of dense hadronic matter such as the quark-gluon plasma and the hot hadronic gas. Due to the small cross sections of electromagnetic interactions, these dileptons, once produced, can escape strongly interacting volumes having sizes which might be produced in heavy-ion collisions. The dilepton invariant mass spectrum contains the most promising signatures of the quark-gluon plasma such as thermal dileptons [39] and the J/ψ suppression [40]. However, the use of the dilepton probe is difficult for an obvious reason: it is sensitive to many different sources. In the low mass region, the resonance decays from the light hadrons constitute the main background. In the intermediate and high mass regions, the Drell-Yan dilepton production from the initial hard scattering is important. In high energy heavy-ion colliders such as RHIC and LHC, the heavy flavor quark production can be quite substantial and its subsequent decay can lead to a large combinatorial background for the dilepton spectrum. Therefore it is crucial to make a solid theoretical prediction on the contribution from heavy quark decays.

The dilepton (dimuon in our case) emission as the decay product of the heavy quarks (charm and bottom) produced in an initial hard scattering and a thermalized quark-gluon medium is calculated at RHIC energy. The next-to-leading order radiative corrections and nuclear shadowing effects are included. The recent work by Gavin, McGaughey, Russkanen and Vogt [41] has indicated that the

dilepton production from the correlated charm decay is by far the dominant contribution. However, if the energetic charmed parton is subject to energy losses due to multiple secondary interactions in the dense matter produced in the collisions, the dilepton spectrum may be considerably softened, as suggested recently by Shuryak [42]. In contrast to the charm, the bottom decay can yield higher invariant mass lepton pairs even at rest due to the large bottom mass. It is thus necessary to examine the various components of the heavy quark spectra and their role in the dilepton production in an extended dilepton mass region. The sensitivities of the perturbative calculation on the choices of the relevant physical scale and the heavy quark fragmentation function are discussed. The heavy parton production is calculated using the explicit next-to-leading order matrix elements, while the parton fragmentation and the heavy hadron decay are handled by the ISAJET Monte Carlo model [43]. The cascade decays of the bottom quark, $b \rightarrow c \rightarrow s$ are also included in this model.

The initial parton differential distributions are calculated using the next-to-leading-order (NLO) matrix elements provided by Nason, Dawson and Ellis in [20, 14]. We have taken $m_c = 1.5$ GeV, $m_b = 4.7$ GeV, and the factorization and renormalization scale μ to be the transverse mass m_T. For charm, however, the factorization scale was taken to be $2m_T$ because the initial virtuality of the MRS A set is $Q^2 = 4$ GeV^2. The nucleon structure function is parameterized by MRS A and the nuclear shadowing fits the EMC, NMC and E665 data [32]. The total cross sections (per initial nucleon) are $\sigma_{c\bar{c}}^{\rm tot} = 153\mu$b and $\sigma_{b\bar{b}}^{\rm tot} = 1.5\mu$b for Au+Au collisions at $\sqrt{s} = 200$ GeV/A. As is evident from Fig. 6.1, the leading order (in heavy quark mass) fragmentation function $D(z) \sim \delta(1-z)$ seems to be a reasonable approximation for heavy quarks. There is some noticeable softening of heavy mesons at large p_t and an enhancement of B-mesons at very small p_t due to the finite heavy quark mass and the heavy quark-hadron mass splitting. The semileptonic decay of the heavy meson can be conveniently handled by Monte Carlo simulations such as ISAJET or JETSET. These Monte Carlo programs usually have the leading order

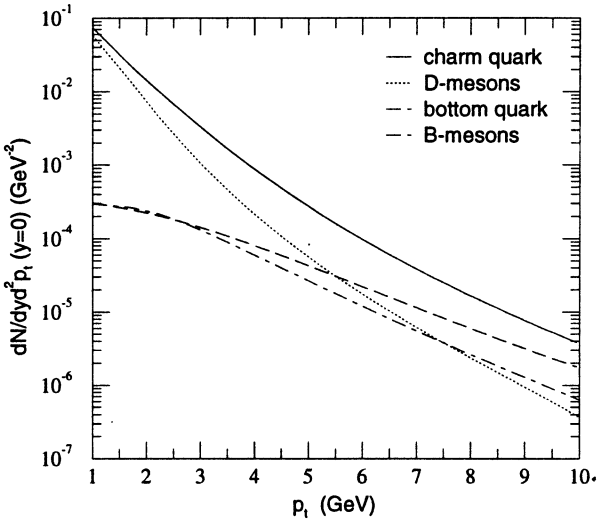

Figure 6.1: The heavy quark hadron differential cross sections calculated using the Peterson heavy quark fragmentation functions convoluted with the parton cross sections. The initial heavy quark productions are calculated using the explicit next-to-leading-order matrix elements with the MRS A structure function and the nuclear shadowing function parameterized by Benesh *et. al.*

matrix elements as the default value while the initial and final state radiations are treated by a parton shower model. The virtue of the parton shower algorithm is that it is beyond the leading logarithmic approximation and incorporates multiple parton emissions. On the other hand, it is not a consistent higher order calculation since it does not contain the virtual corrections in the matrix elements. Simply embedding the NLO matrix elements in the Monte Carlo program may cause an ambiguity due to double counting of multiple parton emissions. To circumvent this difficulty and to preserve the NLO heavy quark production calculation, we developed a numerical routine to generate the events at the parton level. We explicitly integrated out the initial parton momenta in the total cross section Monte Carlo integral and wrote out the four-momentum for each heavy quark. These momenta were associated with the corresponding weight in the phase space multiplied by the corresponding value of the transition probability. Summing up these weights gave the total cross section. One can then use ISAJET to fragment each parton pair and to track the subsequent correlated decays.

When generating events, one encounters a genuine feature of the higher order calculation: the counter events, which arise from the virtual diagrams and the collinear subtraction. In the factorization scheme, one uses the "+ function" prescription to cancel the collinear singularities in the initial state radiation. As a result, the events associated with the counter terms have to be generated in the Monte Carlo integration of the matrix elements. There is no guarantee that the differential cross section should always add up to a positive value everywhere in the presence of the counter events. Some negative bins may appear in the region close to the boundary of phase space for real emission. The problem is worse when one calculates the dilepton spectrum. Due to the statistical nature of the decay process, there is no prediction where the negative bins may appear in the dilepton invariant mass spectrum. In order to make the distribution more readable in the presence of such negative bins, one can always enlarge the size of the these bins so as to integrate over more and more positive real contributions.

The calculated dimuon spectra, at RHIC, from the decay of heavy quarks produced in a hard scattering and in an idealized quark-gluon plasma are plotted in Fig. 6.2. The dimuon spectrum from thermal charm quark production is considerably softer than the initial hard scattering results as can be inferred from the p_t distribution in Fig. 6.1. However, it dominates the dilepton production in the low mass region ($M < 2$ GeV). This can be an important background at RHIC for the dilepton signatures for the low lying vector resonances such as ρ and ϕ. It is important to note that the calculated thermal charm contribution corresponds to a very ideal case where the quarks and gluons are fully equilibrated. The result may be considerably smaller in the plasma where the chemical process is not in equilibrium [36]. The thermal production of the bottom quark is negligible and is not included in Fig. 6.1. The cascade decays of B-mesons, $b \rightarrow c \rightarrow s$ are also included in the curve for the initial fusion bottom production. We have not assumed any secondary interactions in the medium produced in the collision. Though the production rate for the initial bottom quark is much smaller than the charm, the dilepton production from B-meson decay is non-negligible in the large invariant mass region due to the large rest mass of the B-meson. It becomes the dominant contribution when the dimuon invariant mass is above $\sim$ 4 GeV. The results by Gavin *et al.* [41] show a rather small bottom contribution. If the fast charm suffers significant energy loss before it hadronizes, the dimuon spectrum from the initial fusion charm can be considerably softened. In fact, it becomes very similar to that of the thermal charm and falls off rapidly as M gets bigger than 2 GeV, as demonstrated by Shuryak [42]. In this case, the bottom dominance is more prominent and starts at a smaller value of $M \sim 2$ GeV because two B-mesons at rest can produce an energetic lepton pair. To make a comparison, the Drell-Yan dimuon production taken from Ref.[41] is also indicated in the plot.

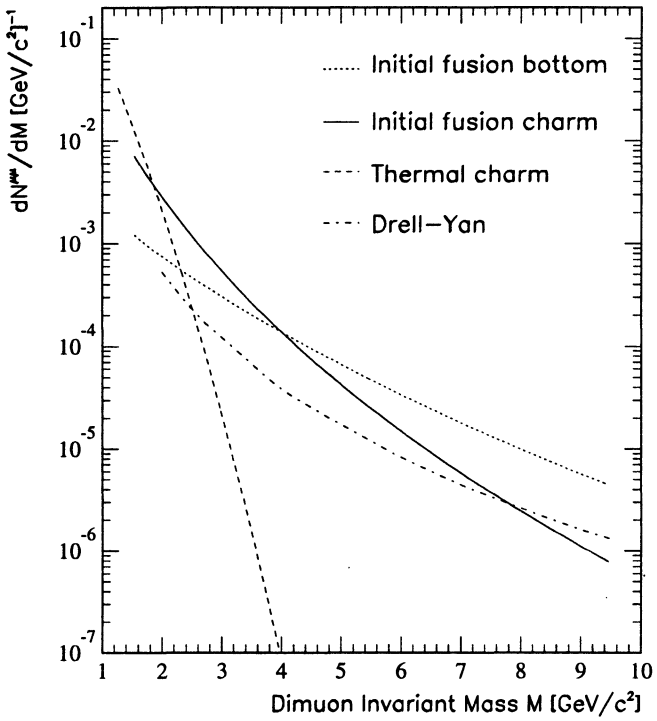

Figure 6.2: The dimuon invariant mass spectra from the correlated heavy quark decay calculated using ISAJET. No energy loss for the fast parton is assumed. The error bars are due to statistics only.

CHAPTER 7

Summary and Conclusions

To summarize, I have presented results for the differential and total inclusive cross sections for charm production in hadronic and heavy-ion collisions at RHIC and LHC energies. These calculations include the next-to-leading order corrections, $O(\alpha_s^3)$, and the nuclear shadowing effect with the assumption that the shadowing effect is the same for the gluon density in a nucleus as the observed effect in the quark distribution [15]. The low-energy data for the total cross section for charm production in p-p and p-A collisions provide some constraints on our theoretical parameters, especially for the choice of the renormalization scale. The choice $Q = m_c$ seems to be preferred by the data. Theoretical uncertainty in the calculation of charm production in nuclear collisions due to the choice of the structure function is small at Fermilab fixed target energies (only few percent) and at RHIC (8% in the central rapidity region), while at LHC energies this uncertainty is about a factor of 6. Furthermore, the shape of the rapidity distribution for charm production in Au-Au collisions at LHC is very sensitive to the low-x behavior of the gluon structure function, resulting in a larger "dip" at $y = 0$ for a more singular function. Similarly, the transverse momentum distribution at LHC is much steeper when obtained with the MRS D– structure function than with less singular structure functions, such as the MRS A set or a non-singular structure function, like the MRS D0 set. For the rapidity distribution, the hadronic K-factor is about 2 (2.5) at RHIC (LHC) energies, while the *effective* K-factor for Au-Au collisions is about 1.5 (1.1). In the p_T distribution, the hadronic K-factor at LHC energies varies from 1.4 at $p_T = 0.7$ GeV to 7.6 at $p_T = 6$ GeV, while the *effective* K-factor changes

	RHIC		LHC	
	p-p	Au-Au	p-p	Au-Au
Total Cross Section or Total Number of $c\bar{c}$ Produced				
$\sigma_c(mb)$ or N_c	0.18	4.0	7.1	110
K-factor	2	1.4	2.4	1.2
Rapidity Distribution				
$\frac{d\sigma_c}{dy}\|_{y=0}$ (mb) $(\frac{dN_c}{dy}\|_{y=0})$	0.042	1.0	0.77	10.4
K-factor	2.0	1.5	2.2	1.3
$\frac{d\sigma_c}{dy}\|_{y=3(5)}(mb)$ $(\frac{dN_c}{dy}\|_{y=3(5)})$	0.01	0.2	0.36	6.75
K-factor	2.1	1.4	2.5	1.1
Transverse Momentum Distribution				
$\pi\frac{d\sigma_c(dN_c)}{d^2p_T}\|_{p_T=1GeV}(mb/GeV^2)$	0.04	1	1.1	17
K-factor	1.7	1.1	1.5	0.7
$\pi\frac{d\sigma_c(dN_c)}{d^2p_T}\|_{p_T=6GeV}$ (mb/GeV^2)	0.0001	0.003	0.013	0.25
K-factor	3.1	3.0	7.6	4.6

Table 7.1: Summary of the open charm production via hard parton scatterings

from 0.6 to 4.6 in the same p_T range. The behavior of the *effective* K-factor is a direct consequence of the fact that the low p_T (small x) region corresponds to the maximum shadowing of the gluon distribution, which in case of gold is about 62%, while the larger values of p_T probe regions of phase space where the nuclear shadowing is smaller. I also present the effective A-dependence for the differential and total cross sections for charm production in p-Au and Au-Au collisions at RHIC and in Au-Au collisions at the LHC. The dominant contribution to charm production comes from the initial state gluons (about 95% at RHIC and 99% at LHC). Thus, combined measurements of inclusive charm production in hadronic and nuclear collisions at these energies, in addition to providing an important test of perturbative QCD in the small-Q^2 and small-x regions, might be able to provide valuable information about the elusive role of gluons inside a nucleus, especially in the region of very small x.

Another calculation of the open charm production cross sections at RHIC and LHC energies for hadronic collisions was performed [18]. The charm yield

	RHIC		LHC	
	p-p	Au-Au	p-p	Au-Au
Total Cross Section or Total Number of $b\bar{b}$ Produced				
$\sigma_b(\mu b)$ or N_c	1.6	.04	190.	3.3
K-factor	2.1	1.7	2.3	1.3
Rapidity Distribution				
$\frac{d\sigma_b}{dy}\|_{y=0}$ (μb) $(\frac{dN_b}{dy}\|_{y=0})$	.5	.01	26	.47
$\frac{d\sigma_b}{dy}\|_{y=3(5)}(\mu b)$ $(\frac{dN_b}{dy}\|_{y=3(5)})$	.01	10^{-4}	6.1	.12
Transverse Momentum Distribution				
$\pi\frac{d\sigma_b(dN_b)}{d^2p_T}\|_{p_T=1GeV}(\mu b/GeV^2)$	0.13	.003	9.6	.15
$\pi\frac{d\sigma_b(dN_b)}{d^2p_T}\|_{p_T=6GeV}$ $(\mu b/GeV^2)$	.078	.0002	1.3	.02

Table 7.2: Summary of the open bottom production via hard parton scatterings

predicted was systematically higher than our calculation, by a factor of 2 or more. This was due to the differences in the choice of scale and heavy quark mass. In our calculation, the charm mass was taken to be 1.5 GeV and then the low energy hadronic data was used to fix the renormalization and factorization scales to be m_c and $2m_c$ respectively. In [18], the renormalization and factorization scales were taken to be $\mu = 2m_T$, and the low energy data was used to fix the charm mass at 1.2 GeV. Both of these calculations are consistent.

The dilepton mass spectra from the decay of the heavy quark produced from the initial hard scatterings and from a quark-gluon plasma for Au+Au collisions were calculated for RHIC energy. We checked the reliability of the leading order results by explicitly performing a next-to-leading-order calculation. The thermal charm from an ideal quark-gluon plasma dominates the dilepton emission in the low dilepton invariant mass region (< 2 GeV). The correlated heavy mesons produced from the initial hard scatterings constitute the major contribution to the intermediate and high mass dileptons. If there is significant energy loss for the fast charm, the bottom decay is by far the dominant component in the intermediate and high dimuon mass regions. In any case, one is likely to find more bottom than charm in the high mass dilepton channel ($M > 4$GeV) at central Au+Au collisions

at RHIC.

APPENDIX A

Structure Functions

In this dissertation, I have discussed the large theoretical uncertainties in the predictions for the heavy quark production at LHC energies due to the unknown low-x behavior of the gluon density in a nucleon and in a nucleus. At these energies, the dominant sub-process for heavy quark production is gluon fusion. Currently there are no direct measurements of a gluon distribution in a nucleus. Furthermore, for the x-values probed at these energies ($x \sim O(10^{-4})$ at rapidity $y \approx 0$ and $x \sim O(10^{-6})$ at rapidity $y \approx 5$) there is also no experimental data on gluon structure function in a nucleon [23]. In our calculation of the heavy quark production in heavy-ion collisions, we have assumed that each parton structure function in a nucleus can be written as the product of a parton structure function in a nucleon and an appropriate function that models the nuclear effects. Since gluon density in a nucleus depends in a non-trivial way on the gluon density in a nucleon, better understanding of the low-x behavior of the gluon density in a hadron *and* in a nucleus is needed.

For the calculation of perturbative QCD processes involving hadronic initial states, the parton model is the most successful approach. In this model, the non-perturbative effect of confinement is encapsulated into a set of quark and gluon structure functions, which depend on the kinematic variables x and Q^2, representing the momentum fraction of the hadron carried by the parton and the virtuality of the probing photon. The most simple parton model description of deep inelastic lepton-hadron scattering leads to the so-called Bjorken Scaling of parton distributions. That is, the structure functions are independent of Q^2 to

first order. However, when higher order QCD corrections are taken into account, such as gluon bremsstrahlung from the initial parton states, the scaling behavior is violated, and the structure function depends logarithmically on Q^2 as well as on x. At large enough Q^2, the expansion parameter, $\alpha_s \sim (\ln Q^2)^{-1}$, is small enough that perturbative QCD (PQCD) is expected to be valid. However, when calculating the bremsstrahlung corrections to deep inelastic scattering, terms of the form $\alpha_s \ln Q^2$ appear, and therefore α_s is not an appropriate expansion parameter. In this case all diagrams which have $(\alpha_s \ln Q^2)^n$ contributions need to be resummed. In the physical (axial) gauge, it has been shown that the dominant contribution comes from ladder diagrams, with strongly ordered transverse momentum [44]. By summing up the parton ladder diagrams, the evolution of parton densities can be described in the large-Q^2 and intermediate-x region by the Gribov-Lipatov-Altarelli-Parisi equations [44, 45]:

$$\frac{dq_i(x,t)}{dt} = 4\pi\alpha_s(Q^2) \sum_{partons} \int_x^1 \frac{dy}{y} P_{ji}(x/y) q_j(x,t) \tag{A.1}$$

where $t = \frac{1}{2}\ln(Q^2/Q_o^2)$ and $P_{ji}(x/y)$ is the probability of finding a parton of type i with momentum fraction x inside a parton of type j with momentum fraction y.

Ladder diagrams with vector particles in the t-channel contain a large $\ln(1/x)$ contributions for each α_s. The resummation of the leading $\alpha_s \ln(1/x)$ terms corresponds to summing gluon ladders. This resummation provides the description of structure function evolution to small-x, through the Balitskii-Fadin-Kuraev-Lipatov equation (BFKL) [46]:

$$\frac{\partial\phi(x,q^2)}{\partial \ln(1/x)} = \frac{N_c\alpha_s}{\pi} \int K(q^2,q'^2)\phi(x,q'^2)\frac{d^2q'}{2\pi}, \tag{A.2}$$

$$\phi(x,q^2) = \frac{\partial xG(x,q^2)}{\partial q^2}, \tag{A.3}$$

and

$$K(q^2,q'^2)\phi(x,q'^2) = \frac{\phi(x,q'^2)}{(q-q')_t^2} - \frac{q_t'^2\phi(x,q^2)}{(q-q')_t^2(q_t'^2+(q-q')_t^2)}, \tag{A.4}$$

where N_c is the number of colors. The first term in the kernel, $K(q^2, q'^2)$, describes the emission of a gluon, and the second term describes the reggeization of all of the t-channel gluons in the ladder. This equation is valid only for small-Q^2 and small-x.

The solution to the BFKL equation increases rapidly at small-x ($xG(x,Q^2) \sim x^{-0.5}$). This behavior is in agreement, although it is on the outer limits of the new HERA data, which can be fitted with [47]:

$$F_2^{exp} \sim (\frac{1}{x})^{\omega_{exp}}, 0.3 < \omega_{exp} < 0.5. \tag{A.5}$$

Thus, the BFKL equation is a reasonably good starting point in the study of low-x physics. However, at small enough x, this singular behavior will result in the violation of the Froissart bound. This violation of unitarity, one of the most important properties of the S-matrix, can be seen in this way. The cross section for a virtual photon interacting with a nucleon must be less than the transverse size of the nucleon:

$$\sigma(\gamma^* N) < \pi R_N^2, \tag{A.6}$$

and this cross section can be written as

$$\sigma(\gamma^* N) = \sigma(\gamma^* g) xG(x,Q^2) \sim \frac{\alpha_s(Q^2)}{Q^2} xG(x,Q^2). \tag{A.7}$$

Taking a gluon density given by the solution to the BFKL equation, we can make an estimate of the kinematic region for which the BFKL solution will not violate unitarity:

$$\frac{\alpha_s(Q^2)}{Q^2}(\frac{1}{x})^{\omega} \leq \pi R_N^2 \tag{A.8}$$

From this equation we can extract a critical line in the $(\ln(1/x), \ln Q^2)$ plane, below which, these perturbative techniques are valid, and above which, these solutions violate unitarity:

$$\ln \frac{1}{x_{cr}} = \frac{1}{\omega} \ln \frac{\pi R_N^2 Q^2}{\alpha_s(Q^2)}. \tag{A.9}$$

For those x-values smaller than x_{cr} the BFKL approach needs to be modified.

The first attempt at modifying this equation was made over a decade ago by Gribov, Levin and Ryskin (GLR) [48]. They have taken into account the parton overlapping effect in dense systems. When partons overlap spatially, there is a chance for parton recombination, which effectively lowers the parton density. They have modified the BFKL equation by adding a non-linear term, corresponding to gluon recombination. This modified BFKL equation is called GLR equation and is given by

$$\frac{\partial\phi(x,q^2)}{\partial\ln(1/x)} = \frac{N_c\alpha_s}{\pi}\int K(q^2,q'^2)\{1-\alpha_s\frac{\phi(x,q'^2)}{\phi_0}\}\phi(x,q'^2)\frac{d^2q'}{2\pi}, \tag{A.10}$$

where $\phi_0 = \frac{32N_c}{9Q_0^2}$. In the Double Log Approximation (DLA), terms containing large $\alpha_s \ln Q^2 \ln(1/x)$ are summed. In the axial gauge, this corresponds to gluon ladders where the t-channel gluons have strongly ordered transverse momenta. The GLR equation also includes multi-ladder "fan" diagrams. In the DLA, the GLR equation can be written as:

$$\frac{\partial^2 xG(x,Q^2)}{\partial\ln\frac{1}{x}\partial\ln Q^2} = \frac{\alpha_s N_c}{\pi}xG(x,Q^2) - \frac{\alpha_s^2\gamma}{Q^2R_N^2}(xG(x,Q^2))^2, \tag{A.11}$$

where $\alpha_s\gamma$ is the three-pomeron vertex coupling, and $\gamma = \frac{81}{16}$ for 3 colors [49].

One of the assumptions of the GLR equation is that the gluons are uniformly distributed on a disc of size R_N, so then, when we define a parameter $\rho \equiv \frac{xG(x,Q^2)}{\pi R_N^2}$, the probability that two gluons have the same value of x and Q^2, denoted $P^{(2)}$, is approximately ρ^2, which appears in the second term on the right side of Eq. (2.11). This is valid only at large x and/or small Q^2. In general, $P^{(2)}$ and ρ^2 are related by [50]:

$$\frac{P^{(2)}}{\rho^2} \propto e^{\frac{1}{(N_c^2-1)^2}\sqrt{\frac{16N_c\alpha_s}{\pi}\ln\frac{Q^2}{Q_0^2}\ln\frac{1}{x}}}, \tag{A.12}$$

where Q_0^2 is the initial virtuality of the cascade, on the order a few GeV. The GLR equation needs to be modified to include two-gluon correlations, $P^{(2)}$, instead of ρ^2.

At smaller values of x, multi-gluon correlations, $P^{(n)}$ becomes important. These multi-gluon correlations are related to the higher-twist terms in the Wilson operator product expansion [51]. To see this we write the gluon structure function using the OPE as:

$$xG(x,Q^2) = xG^{(1)}(x,Q^2) + \sum_n \frac{1}{(QR_n)^{2(n-1)}} x^n G^{(n)}(x,Q^2). \tag{A.13}$$

The n-gluon correlation is related to the twist-$2n$ term in the OPE by $P^{(n)} = \frac{x^n G^{(n)}(x,Q^2)}{(\pi R_N^2)^n}$. In analogy to the GLR equation, evolution equations for the n-gluon correlations can be written as [52]:

$$\frac{\partial^2 P^{(n)}(x,Q^2)}{\partial \ln\frac{1}{x} \partial \ln Q^2} = \gamma_{2n}\omega P^{(n)}(x,Q^2) - n\frac{\alpha_s^2 \gamma \pi}{Q^2} P^{(n+1)}(x,Q^2), \tag{A.14}$$

where γ_{2n} is the anomalous dimension of the twist-$2n$ quasi-partonic operator, $\omega = N-1$, and N is the Mellin-conjugate variable to x. The anomalous dimension calculated in DLA approximation is given by [53]:

$$\gamma_{2n} = \frac{\overline{\alpha}_s n^2}{\omega}\{1 + \frac{\delta^2}{3}(n^2-1)\}, \tag{A.15}$$

where $\overline{\alpha}_s = \frac{\alpha_s N_c}{\pi}$ and $\delta = (N_c^2-1)^{-1}$.

Laenen and Levin [52] combined this infinite set of coupled differential equations into one differential equation. They start by defining a generating function:

$$g(x,Q^2,\eta) = \sum_{n=1}^{\infty} e^{n\eta} x^n G^{(n)}(x,Q^2). \tag{A.16}$$

The gluon density can be obtained from the generating function by:

$$xG(x,Q^2) = Q^2 R_N^2 g(x,Q^2,\eta = -\ln(Q^2 R_N^2)). \tag{A.17}$$

Then, the equations (2.14) can be written in the following form:

$$\frac{\partial^2 g(x,Q^2,\eta)}{\partial \ln\frac{1}{x} \partial \ln Q^2} = \overline{\alpha}_s \frac{\partial^2 g}{\partial \eta^2} + \frac{\overline{\alpha}_s \delta^2}{3}\left(\frac{\partial^4 g}{\partial \eta^4} - \frac{\partial^2 g}{\partial \eta^2}\right) - \alpha_s^2 \gamma e^{-\ln(Q^2 R_N^2)} e^{-\eta}\left(\frac{\partial g}{\partial \eta} - g\right). \tag{A.18}$$

This equation is a fourth-order PDE in 3 dimensions and it is difficult to solve. It is interesting to note that R_N is a parameter that can not exceed the size of

the hadron, but it could also be related to the size of localized regions of high gluon density, so-called hot spots. Since this equation takes into account multi-gluon correlations it is appropriate for dense nuclear systems, provided appropriate boundary and initial conditions are used.

REFERENCES

[1] J.D. Bjorken, *Phys. Rev.* **D27**, 140 (1983).

[2] R. Albrecht *et al.*, WA80 Collaboration, *Zeit. Phys.* **C55**, 539 (1992).

[3] A. Chados, R.L. Jaffe, K. Johnson, C.B. Thorn and V.F. Weisskoppf, *Phys. Rev.* **D9**, 3471 (1974).

[4] P.V. Ruuskanen, *Nucl. Phys.* **A544**, 169c (1992).

[5] R. Vogt, B.V. Jacak, P.L. McGaughey, and P.V. Ruuskanen, *Phys. Rev.* **D49**, 3345 (1994).

[6] A. Shor, *Phys. Lett.* **B215**, 375 (1988).

[7] A. Shor, *Phys. Lett.* **B233**, 231 (1989).

[8] E. Shuryak, *Yad. Fiz.* **28**, 796 (1978).

[9] E. Shuryak, *Phys. Rev. Lett.* **68**, 3270 (1992).

[10] L. Cambridge, J. Kripfganz, and J. Ranft, *Phys. Lett.* **70**, 234 (1977).

[11] E. Shuryak, *Zh. Eksp. Teor. Fiz.* **74**, 408 (1978).

[12] H. Cobbaert *et al.*, *Phys. Lett.* **B206**, 546 (1987).

[13] B. Müller and X.-N. Wang, *Phys. Rev. Lett.* **68**, 2437 (1992).

[14] M.L. Mangano, P. Nason and G. Ridolfi, *Nucl. Phys.* **B373**, 295 (1992).

[15] NMC Collaboration, P. Amaudruz *et al.*, *Z. Phys.* **C51**, 387 (1991); E665 Collaboration, M.R. Adams *et al.*, *Phys. Rev. Lett.* **68**, 3266 (1992); EMC

Collaboration, J. Ashman *et al.*, *Phys. Lett.* **B202**, 603 (1988); M. Arneodo *et al.*, *Phys. Lett.* **B211**, 493 (1988).

[16] I. Sarcevic and P. Valerio, *Phys. Lett.* **B338**, 426 (1994); I. Sarcevic and P. Valerio, *Phys. Rev.* **C51**, 1433 (1995).

[17] D. Fein, Z. Huang, P. Valerio and I. Sarcevic, hep-ph/9607246, submitted to *Phys. Lett.* **B**.

[18] R.V. Gavai, S. Gupta, P.L. McGaughey, E. Quack, P.V. Ruuskanen, R. Vogt and X.-N. Wang, *Int. J. Mod. Phys.* **A10**, 2999 (1995).

[19] Z.-w. Lin. and M. Gyulassy, *Phys. Rev.* **C51**, 2177 (1995): Erratum *ibid.* **C52**, 440 (1995).

[20] P. Nason, S. Dawson and R.K. Ellis, *Nucl. Phys.* **B327**, 49 (1989); *ibid. Nucl. Phys.* **B303**, 607 (1988).

[21] W.A. Bardeen, A. Buras, D.W. Duke and T. Muta, *Phys. Rev.* **D18**, 3998 (1978).

[22] J. Collins, F. Wilczek and A. Zee, *Phys. Rev.* **D18**, 242 (1978).

[23] G. Wolf, *Nucl. Phys. Proc. Suppl.* **38**, 107 (1995).

[24] A.D. Martin, W.J. Stirling and R.G. Roberts, *Phys. Rev.* **D47**, 867 (1993).

[25] A.D. Martin, W.J. Stirling and R.G. Roberts, *Phys. Rev.* **D50**, 6734 (1994).

[26] S. Aoki *et al.*, *Phys. Lett.* **B224**, 441 (1989); S.P.K. Tavernier, *Rep. Prog. Phys.* **50**, 1439 (1987); S. Barlag *et al.*, *Z. Phys.* **C39**, 451 (1988).

[27] For a review of the future plans for high precision charm measurements see D.M. Kaplan, *Nucl. Phys. Proc. Suppl.* **50**, 260 (1996).

[28] For a recent review of the factorization theorems in perturbative QCD see J.C. Collins, D.E. Soper and G. Sterman, in *Perturbative Quantum Chromodynamics*, ed. A.H. Mueller (World Scientific, Singapore, 1989).

[29] K. J. Eskola, K. Kajantie and J. Lindfors, *Nucl. Phys.* **B323**, 37 (1989).

[30] A. Bohr and B.R. Mottelson, *Nuclear Structure I* (Benjamin, New York, 1969) pp. 160.

[31] L. Durand and H. Pi, *Phys. Rev.* **D38**, 78 (1988).

[32] J. Qiu, *Nucl. Phys.* **B291**, 746 (1987); K.J. Eskola, *Nucl. Phys.* **B400**, 240 (1993).

[33] C.J. Benesh, J. Qiu and J.P. Vary, *Phys. Rev.* **C50**, 1015 (1993).

[34] K.J. Eskola, J.-W. Qiu, and X.-N. Wang, *Phys. Rev. Lett.* **72**, 36 (1994).

[35] T.S. Biro, E. van Doorn, B. Muller, M.H. Thoma, and X.-N. Wang, *Phys. Rev.* **C48**, 1275 (1993).

[36] P. Levai, B. Müller and X.-N. Wang, *Phys. Rev.* **C51**, 3326 (1995).

[37] E. Braaten and R.D. Pisarski,*Nucl. Phys.* **B337**, 569 (1990).

[38] T.S. Biro, B. Müller and X.-N. Wang, *Phys. Lett.* **B283**, 171 (1992).

[39] E. Shuryak, *Phys. Lett.* **B78**, 150 (1978).

[40] T. Matsui and H. Satz, *Phys. Lett.* **B178**, 416 (1986).

[41] S. Gavin, P.L. McGaughey, P.V. Ruuskanen and R. Vogt, LBL Preprint LBL-37981 (1996).

[42] E. Shuryak, nucl-th/9605011 (1996).

[43] F.E. Paige, S.D. Protopopescu,*Physics of the Superconducting Supercollider, Snowmass, 1986 : Proceedings*, eds. R. Donaldson and J. Marx (Amer. Phys. Soc., 1988).

[44] V. Gribov and L. Lipatov, *Sov. J. Nucl. Phys.* **15**, 438 (1972).

[45] G. Altarelli and G. Parisi, *Nucl. Phys.* **B126**, 298 (1977).

[46] E. Kuraev, L. Lipatov and V. Fadin, *Sov. Phys. JETP* **45**, 199 (1977); Ya. Balitskii and L. Lipatov, *Sov. J. Nucl. Phys.* **28**, 822 (1978): L. Lipatov, *Sov. Phys. JETP* **63**, 904 (1986).

[47] H1 Collaboration, T. Ahmed *et al.*, *Nucl. Phys.* **B439**, 471 (1995); ZEUS Collaboration, M. Derrick *et al.*, *Phys. Lett.* **B345**, 576 (1995).

[48] L. Gribov, E. Levin and M. Ryskin, *Phys. Rep.* **100**, 1 (1983).

[49] A. Mueller and J. Qiu, *Nucl. Phys.* **B268**, 427 (1986).

[50] J. Bartels, *Z. Phys.* **C60**, 471 (1993); *Phys. Lett.* **B298**, 204 (1993); E. Levin, M. Ryskin and A. Shuvaev, *Nucl. Phys.* **B387**, 589 (1992).

[51] R. Ellis, W. Furmanski and R. Petronzio, *Nucl. Phys.* **B207**, 1 (1982); **B212**, 29 (1983); A. Buhkvostov, G. Frolov and L. Lipatov, *Nucl. Phys.* **B258**, 601 (1985).

[52] E. Laenen and E. Levin, *Nucl. Phys.* **B451**, 207 (1995).

[53] E. Laenen, E. Levin and A. G. Shuvaev, *Nucl. Phys.* **B419**, 39 (1994).